

Title of my master thesis

Franziska Hellmuth



Thesis submitted for the degree of
Master in Meteorology
60 credits

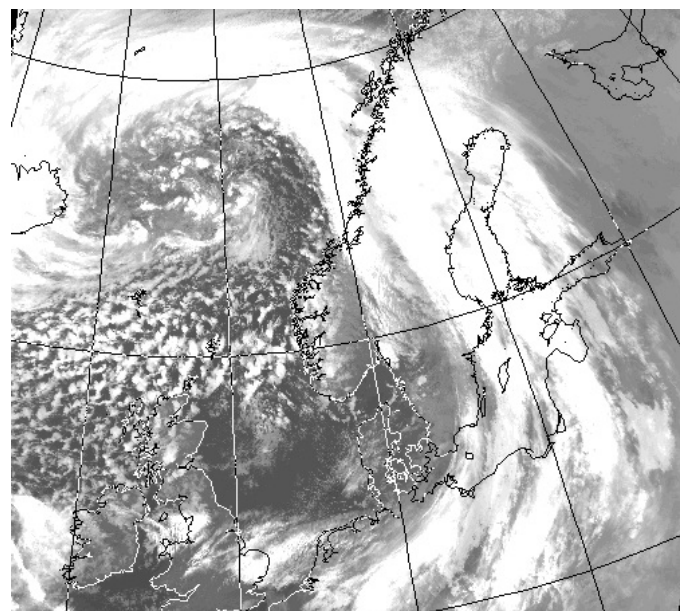
Department of Geoscience
Faculty of Mathematics and Natural Sciences

UNIVERSITY OF OSLO

Spring 2018

Title of my master thesis

Franziska Hellmuth



© 2018 Franziska Hellmuth

Title of my master thesis

<http://www.duo.uio.no/>

Printed: X-press printing house

ABSTRACT

This abstract needs to be updated.

TABLE OF CONTENTS

LIST OF ABBREVIATIONS	III
CHAPTER 1: INTRODUCTION	1
1.1 Measurement site - Haukeliseter	3
1.2 Observations in December	5
1.3 Preliminary MEPS and observation results	5
CHAPTER 2: THEORY	9
2.1 Extratropical Cyclones	9
2.2 Ice formation	10
2.3 Bergeron-Findeisen effect	10
CHAPTER 3: METHODS	11
3.1 Instruments	11
3.1.1 Double Fence	13
3.1.2 MRR - Micro Rain Radar	14
3.1.3 PiP - Precipitation Imaging Package	16
3.1.4 MASC - Multi-Angular Snowfall Camera	17
3.2 Optimal Estimation Retrieval Algorithm	17
3.2.1 Present snow	18
3.2.2 Size distribution	20
3.2.3 Snowfall retrieval scheme	20
3.2.4 Forward model	23
3.2.5 Snowfall rate at the surface	25
3.3 Numerical forecast model	25
3.3.1 AROME - MetCoOP	26
3.3.2 Meso-NH and the ICE3 scheme	26
3.3.3 Adjustment of ICE3 inside MEPS	30
3.4 Data processing	30

3.4.1	Layer thickness in MEPS	30
3.4.2	Snow water content	31
3.4.3	Snow water path	32
3.4.4	Dew point temperature for Skew-T log-P Diagram	32
CHAPTER 4: ANALYSIS OF THE CHRISTMAS STORM 2016		33
4.1	Extreme weather	33
4.2	Dynamic Tropopause map	34
4.3	Thickness, Sea level pressure, moisture, and wind at 250 hPa	37
4.4	Atmospheric River map	39
4.5	Observations at the weather mast	41
4.6	Radiosonde from Stavanger	43
4.7	Large scale circulation	43
CHAPTER 5: RESULTS		47
5.1	Surface snowfall accumulation	48
5.2	SWP and relation to wind	50
5.3	SWC and SWP from MEPS and the optimal estimation retrieval	51
5.4	Wednesday, 21 December 2016	52
5.5	Thursday, 22 December 2016	52
5.6	Saturday, 24 December 2016	52
5.7	Saturday, 25 December 2016	52
REFERENCES		62
APPENDIX A: SCATTERING MODEL		69
APPENDIX B: SKEW-T LOG-P DIAGRAM FROM STAVANGER		71
APPENDIX C: LWC FROM MEPS		75

LIST OF ABBREVIATIONS

AR	Atmospheric River
AROME	Applications of Research to Operations at Mesoscale
C3VP	Canadian CloudSat-CALIPSO Validation Project
CPR	Cloud Profiling Radar
DT	Dynamic Tropopause
ECMWF	European Centre for Medium-Range Weather Forecasts
EPS	Ensemble Prediction System
FMI	Finnish Meteorological Institute
IVT	Integrated Vapour Transport
MASC	Multi-Angular Snowfall Camera
MEPS	MetCoOp Ensemble Prediction System
Meso-NH	Mesoscale Non-Hydrostatic model
Met-Norway	Norwegian Meteorological Institute
MetCoOp	Meteorological Co-operation on Operational NWP
MRR	Micro Rain Radar
MSLP	Mean Sea Level Pressure

NWP	Numerical Weather Prediction
PIP	Precipitation Imaging Package
PSD	Particle Size distribution
SMHI	Swedish Meteorological and Hydrological Institute
SWC	Snow Water Content
SWP	Snow Water Path
WCB	Warm Conveyor Belt
WMO	World Meteorological Organization

CHAPTER 1: INTRODUCTION

The overleaf file from the Introduction is here:

<https://www.overleaf.com/13946064tcvpbpwjzjnk>

During Christmas 2016 a storm impinged on the west coast of Norway. The storm, called 'Urd' was according to [Olsen and Granerød \[2017\]](#) associated with strong winds and high precipitation amounts. The midwind along the coast of Western Norway had hurricane strength (observed: 40 ms^{-1} to 55 ms^{-1}). In South and Eastern Norway west to north-west winds between 25 ms^{-1} to 40 ms^{-1} were measured. At the Haukeliseter measurement site, 136.4 mm of precipitation were monitored during 21 December 2016 to 27 December 2016. This event was just above the limit of been called an extreme weather. Storms of this kind are expected to occur on average every five years [[Olsen and Granerød, 2017](#)].

The financial costs associated with 'Urd' are estimated to about 180 million Norwegian kroner. 'Urd' led to major traffic problems for cars, trains, ferries and air planes. Most mountain crossings were kept closed during Christmas 2016. In addition, there was a power breakout of around 70.000 households and 40 emergency power stations failed during the extreme weather.

This extreme weather, might not have lead to the same damages as some of the extreme weather events of recent years. But since people are affected by extreme weather (Figure 1.0.1) it is important to predict storms, associated precipitation and wind as accurately as possible. Having accurate observations, will lead to better performing models which rely on observations. [include a reference here](#)

Figure 1.0.1 shows that precipitation and strong winds can influence in certain ways the infrastructure. To predict and measure snowfall accumulation as accurately as possible is important since snowfall has impact on avalanches, freshwater release into water systems

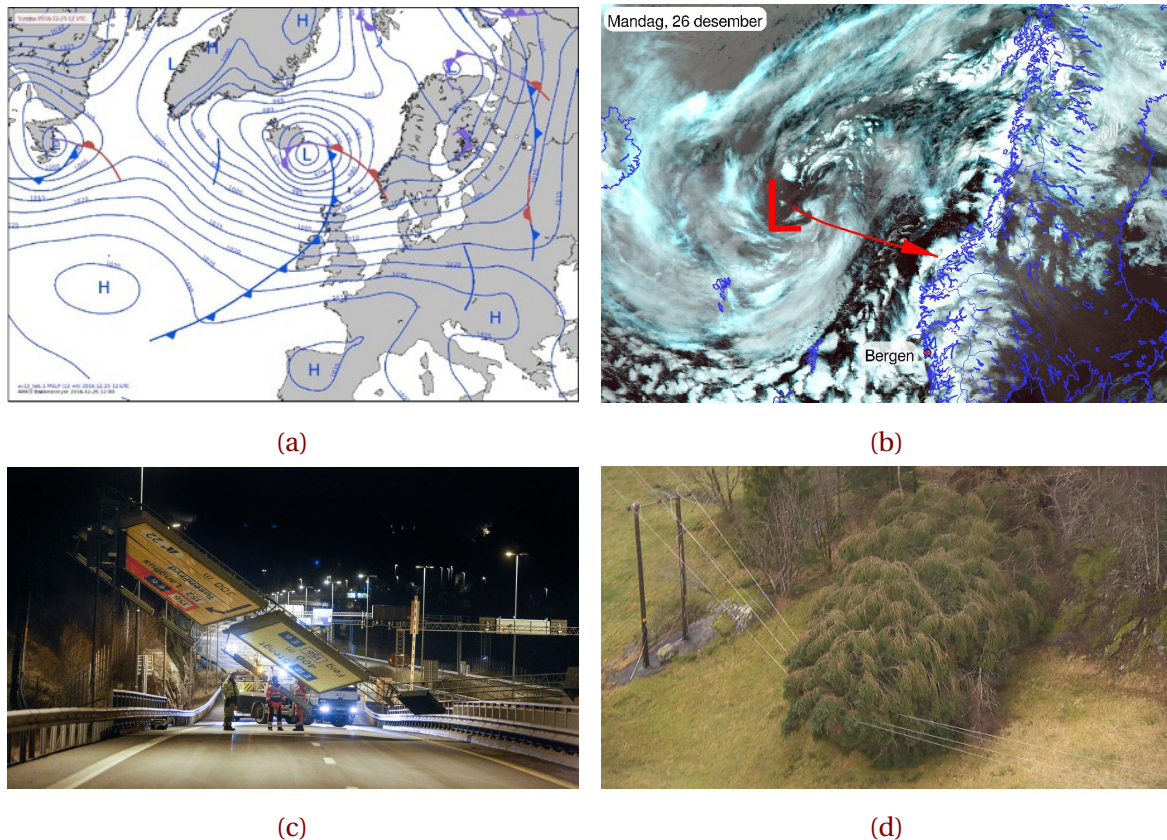


Figure 1.0.1: In a: Weather situation Sunday 25 December 2016 at 12 UTC, [Olsen and Granerød, 2017]. b: Tweet from Meteorologene [2016]: Here comes #Urd! The low pressure centre will hit Møre og Romsdal, but the strongest wind comes south of Stad. #SørNorge. c: This traffic sign, ten meter long and four meter high was blown down during the storm, [Ruud et al., 2016]. d: Trouble maker: The extreme weather during Christmas created problems for the local infrastructure. 80.000 households were without electricity during the storm, [Farestveit, 2016].

in spring, and extra economical expenses for local infrastructure as well as climatological effects.

Joos and Wernli [2012] investigated the influence of microphysical processes on potential vorticity development in warm conveyor belts (WCB). They demonstrated the complex interaction between the small-scale microphyiscal processes and the large-scale flow in WCB. For the understanding of numerical simulations of storm developments it is import-

ant to know vertical precipitation profiles and their position within the synoptic vorticity environment. It is therefore crucial to study the vertical structure of different synoptic storms and predict as accurately as possible.

Since November 2016, the Meteorological Cooperation on Operational Numerical Weather Prediction (MetCoOP) Ensemble Prediction forecast (MEPS) is operational at the Meteorological Institute of Norway (Met-Norway). The study by Müller et al. [2017] shows that the AROME-MetCoOp, a version of the Météo-France Applications of Research to Operations at Mesoscale, performs well for certain meteorological phenomena.

Microphysical processes in weather models are still not well understood and therefore are mostly parametrised [Müller et al., 2017]. Furthermore, high latitude regions are not well represented in meteorological models. Indeed a comparison between the MEPS data fit the observations for December 2016 but uncertainties are still present for this time period. Some satellites, such as CloudSat have been equipped with radar to estimate snowfall rates and vertical profiles of precipitation. CloudSat is one of the satellites orbiting in the A-Train formation and measures the vertical structure of cloud systems [Stephens et al., 2002].

Studies of Kulie and Bennartz [2009] showed that the Cloud Profiling Radar (CPR), mounted on the CloudSat, can be used to estimate global distributions of snowfall. They showed that different combinations of microphyiscal habits and fall speed can lead to the same results of reflectivity and therefore to the same amount of snowfall rate. Methods like optimal estimation retrieval were established to reduce the non-uniqueness. Where ground observations are used to estimate vertical profiles of precipitation.

The improvement of the CloudSat retrieval is helpful to show that climate models over estimate present-day Antarctic snowfall [Palerme et al., 2017]. Norin et al. [2015] presented a good agreement between the ground-based snowfall measurements and satellite observations.

1.1 MEASUREMENT SITE - HAUKELISETER

Haukeliseter, shown in Figure 1.1.1 is a mountain plateau 991 m above sea level, located in the Norwegian county 'Telemark' (59.8° N, 7.2° E, Figure 1.1.1). The station measures precipitation, temperature, snow depth and wind. It has served as a measurement site for

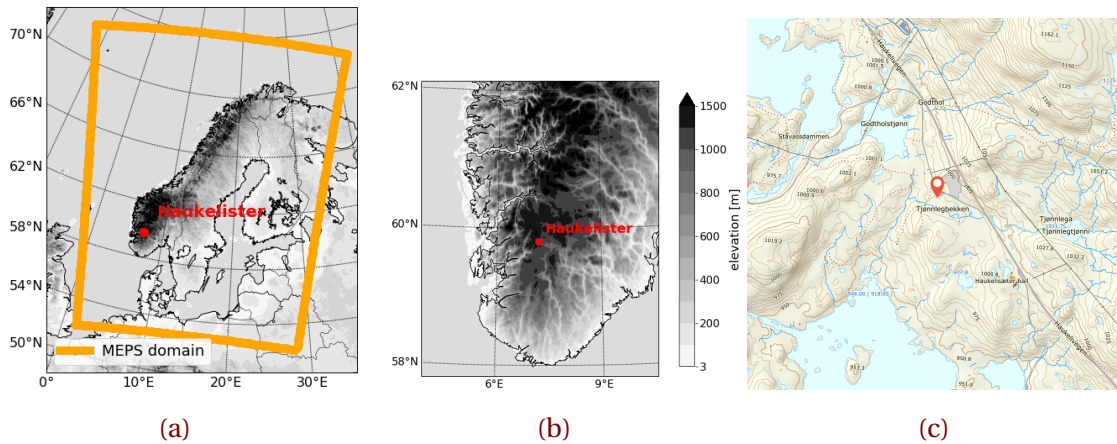


Figure 1.1.1: Elevation map of Northern Europe (a) and South Norway (b). Red dot indicates the location Haukeliseter and the orange square in a indicates the model domain of MEPS. Elevation according to the shading. c: topographical map of the measurement site marked with a red pin [Kartverket, 2018].

snow accumulation since the winter of 2010/2011 [Wolff et al., 2010, 2013, 2015].

The study site is surrounded by mountain tops being 100 m to 500 m higher than the flat area. As seen in Figure 1.1.1c is the Haukeliseter measurement site located between two lakes, furthermore is it more open to the south and the west and the closest mountaintop (situated to the NE) has an altitude of 1162 masl, [Wolff et al., 2015].

In a study by Wolff et al. [2015] the wind-induced under-catch of solid precipitation is determined. Dependent on the kind of precipitation the wind plays different roles in the amount of accumulation. For temperatures below -2°C the wind speed influences the falling snow. Where less precipitation can be observed at higher wind speeds or more precipitation can be measured if too much is blown into the gauge. The catch ratio between the standard Geonor precipitation gauge and the DF-Geonor shows, that only 80 % of solid precipitation are observed at wind speeds of 2 m s^{-1} and only 40 % at 5 m s^{-1} , [Figure 5 in Wolff et al., 2015]. The double fence gauge is more accurate than the single fence and is used as the reference gauge. A further description of the double fence is found in Section 3.1.1. Nevertheless, this shows the need of a combination of ground based observations together with an optimal estimation retrieval to verify the accuracy of MEPS. Wolff et al. [2015] introduced an adjustment function for the Geonor double fence, so that different precipitation under certain wind speeds are presented correctly and can be used

as confidential data.

1.2 OBSERVATIONS IN DECEMBER

The general climate at Haukeliseter can be defined with the updated Köppen-Geiger climate types presented in [Peel et al. \[2007\]](#). Figure 8 in [Peel et al. \[2007\]](#) shows, that Haukeliseter may lay in a transition zone and can be categorized as ET, a polar tundra climate type (hottest month temperature $T_{hot} \geq 0^{\circ}\text{C}$) or Dfc, a cold climate without dry season and cold summers.

Haukeliseter presents a typical Norwegian climate condition. At the measurement site, frequent snow events combined with high wind speeds are observed during a six to seven month winter period. In addition a snow amount of about 2 m to 3 m can be expected, where 50 % of the yearly precipitation is solid [[Wolff et al., 2010, 2013, 2015](#)].

The mean wind direction for solid precipitation is from the west/east with maximum wind speeds above 15 m s^{-1} , observed during a 10 year winter period at a nearby station [[Wolff et al., 2010, 2015](#)]. As seen in Figure 1.2.1 is the average December temperature -6°C (30-yr period 1961 to 1990, value taken from [eklima \[2016\]](#)). December 2016 was warmer with an anomaly of +4.9 K above the climate mean. In 2016, the precipitation was 200 % more than the climate mean. [yr.no says something different. According to them was it only 76 %. But! change to double fence must have changed the precipitation amount to twice as much. Therefore probably wrong climate statistics since measured with single fence.](#)

The precipitation observed in the time period 21 December 2016 to 27 December 2016 where 56.9 % of the total accumulation in December 2016. Furthermore, a maximum wind of 22.3 m s^{-1} was observed in this period, which can be associated to a slight storm, which is further described in Section 4.5 and Table 4.5.1.

1.3 PRELIMINARY MEPS AND OBSERVATION RESULTS

As MEPS is operational since November 2016 one can compare the ensemble forecast model output with observations from the double fence at Haukeliseter. This will later on be compared to the vertical optimal snowfall retrieval estimates.

During Christmas 2016 a storm approached the Haukeliseter site, which resulted in precip-

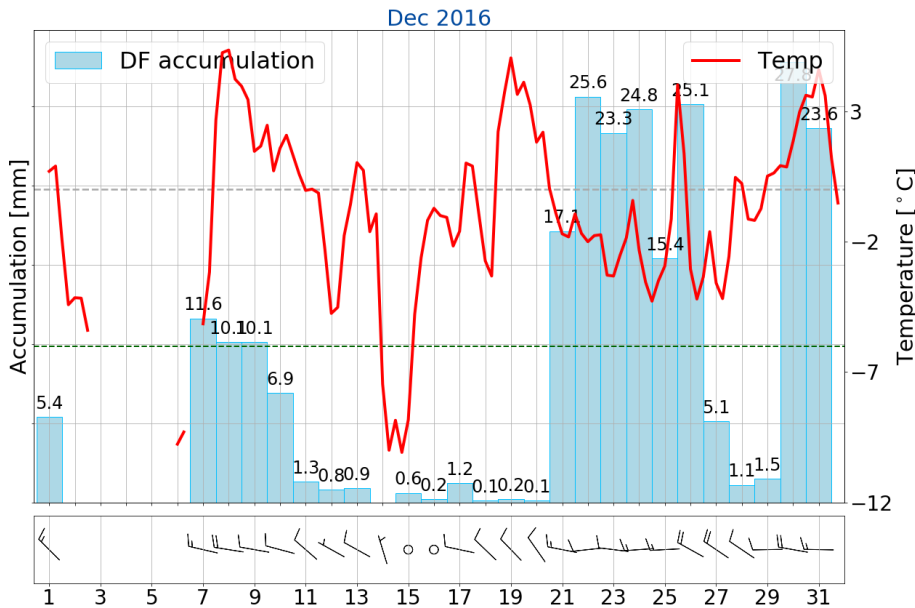


Figure 1.2.1: Observations at Haukeliseter weather mast for December 2016. Daily accumulation [mm] in light blue, mean temperature every six hours (red, [°C]), and daily maximum wind as barbs [m s^{-1}]. Gray dashed line indicates the freezing temperature. The monthly normal value is green dashed (-6.0°C), the values are taken from [eklima \[2016\]](#). Note, that no data was available from 2 December 2016 and 6 December 2016

itation in form of liquid and solid. Figure 1.3.1 shows the preliminary comparison between the MEPS ensemble member forecasts as well as the snowfall accumulation measured by the double fence at Haukeliseter. The double fence data is noisy and therefore, a filtered dataset is accessed from [eklima \[2016\]](#).

Each MEPS cycle is initialized at 18 UTC for the respective day. Grey lines in Figure 1.3.1 show the nine perturbed ensemble members of MEPS. Where the black line reflects the control run, and the dots accumulation by the double fence.

During the first few days the ensemble outputs cover the amount of snow good in comparison to the double fence observations. The spread of the ensemble members around the control run fits as well to the observations for this time period. But, for an initialisation on the 24 December 2016, 18 UTC one can see that MEPS over estimates the amount of snow accumulation. It is even more pronounced with the initialisation on the 25 December 2016, 18 UTC (compare Figure 1.3.1f).

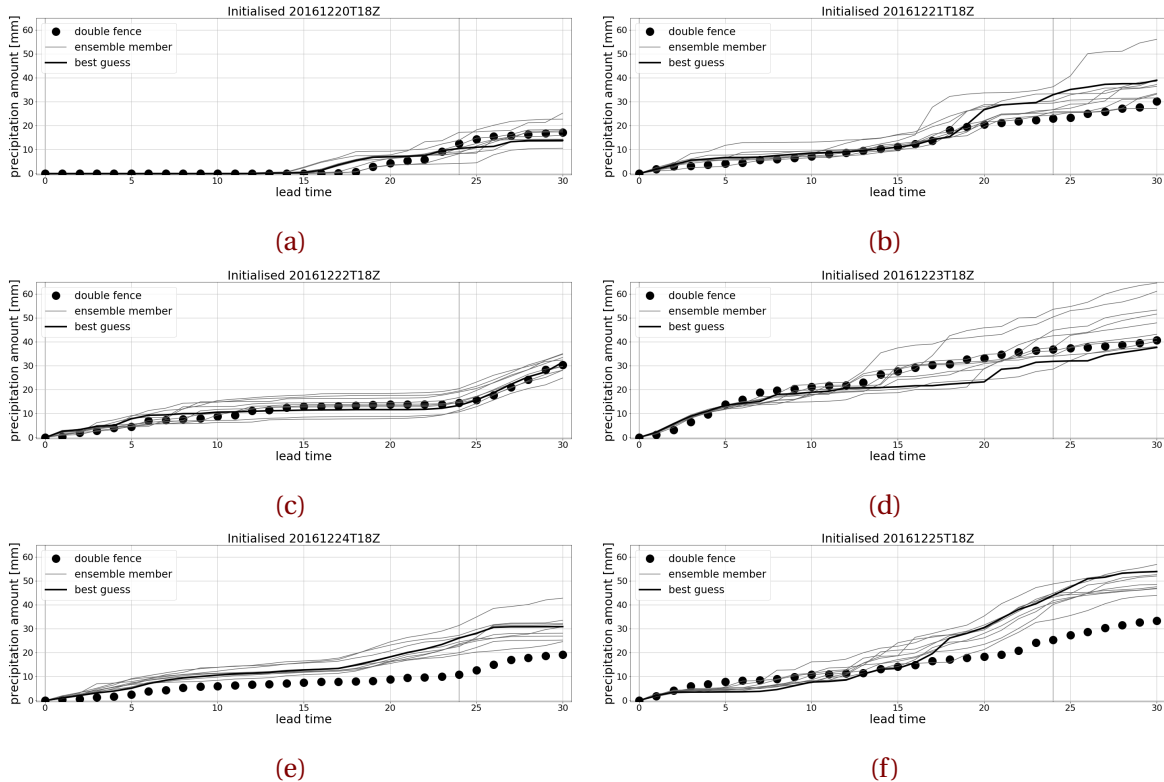


Figure 1.3.1: Accumulation of precipitation at Haukeliseter. Initialisation of MEPS at 18 UTC. Ensemble member as line in grey and the control in black. Dots indicate the hourly accumulation observed at the double fence, [eklima, 2016]. **Do you think I have to make something bigger???** Font size etc? Or use one page only for the figures and have them underneath each other?

This can have different reasons. One of them can be that the large scale weather situation was more predictable for the first four days (Figures 1.3.1a to 1.3.1d). According to Müller et al. [2017] are strong precipitation events better predicted with MEPS than ECMWF (European Centre for Medium-Range Weather Forecasts). On the other side, Müller et al. [2017] states, that an overestimation appears, where the precipitation event (12 h accumulation) is less than 10 mm. This is not the case for the time period 21 December 2016 to 26 December 2016 (compare Figure 1.2.1), where the daily precipitation exceed 10 mm every day. The question arises why MEPS covers the high amount of snow accumulation on the 24 December 2016 but forecasts 24 h prior to 25 December 2016 and 26 December 2016

are not covering the predicted amount of accumulation!

CHAPTER 2: THEORY

The overleaf file from the Methodology is here:

<https://www.overleaf.com/15461164zgrsztkgnfzd>

- What is attenuation?
- Snow formation and different particles. What was observed at Haukeli?
- Rayleigh scattering & Radars [Lohmann et al., 2016, p.257, Sec. 9.3.1]

2.1 EXTRATROPICAL CYCLONES

Markowski and Richardson [2011] ' midlatitude synoptic-scale motions are arguably solely driven by baroclinic instability; extratropical cyclones are the dominant weather system of midlatitudes on the synoptic scale. Baroclinic instability is most likely to be realized by disturbances.'

Extratropical highs and lows have a time-scale of several days and the horizontal extension of several kilometre.

Extratropical cyclones develop with the formation of fronts.

'The destabilization of layers via the potential instability mechanism is probably important in the formation of mesoscale rainbands within the broader precipitation shields of extratropical cyclones on some occasions, especially when potentially unstable layers are lifted over a front. Potential instability also is often cited as being important in the development of deep moist convection.' 'Despite the common presence of potential instability, however, it usually does not play a role in the destabilization of the atmosphere that precedes the initiation of convection.'

'Not only are synoptic fronts and their associated baroclinity important for the development of larger-scale extratropical cyclones, but in some situations even mesoscale boundaries can influence larger-scale extratropical cyclones.'

'In the Norwegian cyclone model, the cold front moves faster than the warm front, eventually overtaking it, resulting in occlusion of the extratropical cyclone, with the occluded front being the surface boundary along which the cold front has overtaken the warm front.'

2.2 ICE FORMATION

Lohmann et al. [2016]

2.3 BERGERON-FINDEISEN EFFECT

CHAPTER 3: METHODS

The overleaf file from the Methodology is here:

<https://www.overleaf.com/13946091vphmgxbxpyg>

This chapter describes the instruments, the optimal estimation retrieval and the regional forecast model used in the scope of this study, to determine the snow water content in the vertical. The determination of required parameters from the measuring instruments in relation to the optimal estimation retrieval will be explained. The purpose of this study is to compare the vertical observations from the Haukeliseter measurement site and the output from the operational forecast model at the Norwegian Meteorological Institute for the extreme weather event during Christmas 2016. The last section will give an insight on how the data was analysed to compare the different systems.

3.1 INSTRUMENTS

Many factors such as humidity and temperature contribute to snowflake geometry. The knowledge of snowflake habits, particle size distributions, and fall speed lead to a reduction of errors in optimal estimation retrievals.

This work is based on several datasets collected at the Haukeliseter measurement site, 59.8° N, 7.2° E. A composition of advanced ground based observations and the CloudSat precipitation retrieval will help to get a better understanding of the vertical structure of the atmosphere.

A collaboration between the University of Utah, University of Wisconsin and Met-Norway made it possible to install three additional instruments at the measurement site during winter 2016/2017. A Multi-Angle Snowflake Camera (MASC) and a Precipitation Imaging Package (PiP) will be used to determine the snow habit, the snowfall particle size distribu-

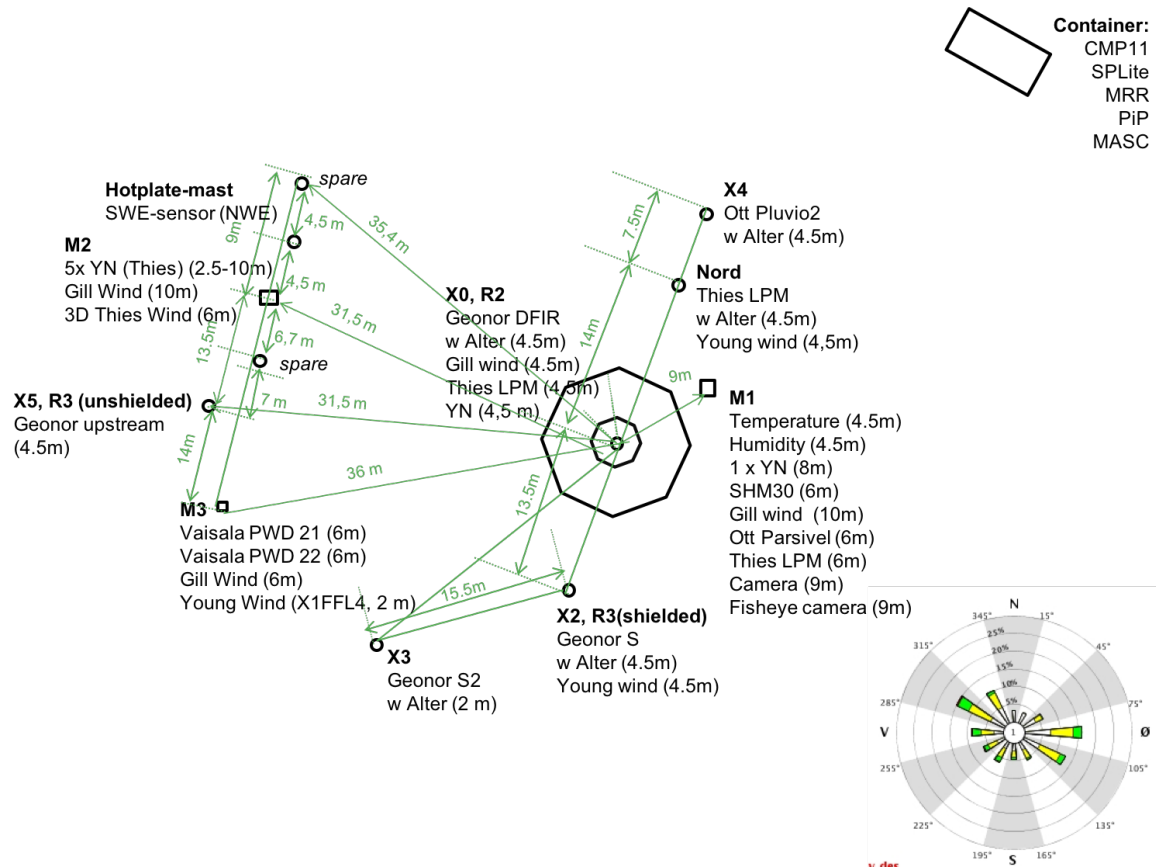


Figure 3.1.1: Instruments at the Haukeliseter measurement site during winter 2016/2017 [adapted from Wolff et al., 2015]. The windrose indicates the mean wind direction from either from west-north-west or east-south-east.

tion, and near-surface fall speed. Additionally, a Micro Rain Radar (MRR) is established to obtain fall speed and particle reflectivity aloft. Together with temperature observations at the surface, is this a good basis to reduce the non-uniqueness of snow accumulation in optimal estimation snowfall retrieval, described in Section 3.2.

A sketch of the instrumentation setting is presented in Figure 3.1.1. The octagonal indicates the double fence. The container is north-east from the double fence having the MRR, MASC and PiP mounted at the top. M1 in Figure 3.1.1 is the 10 m weather mast, providing the hourly [eklima](#) [2016] temperature and wind measurements. The mean wind direction from west-north-west and east-south-east are shown in the windrose in Figure 3.1.1.

3.1.1 DOUBLE FENCE

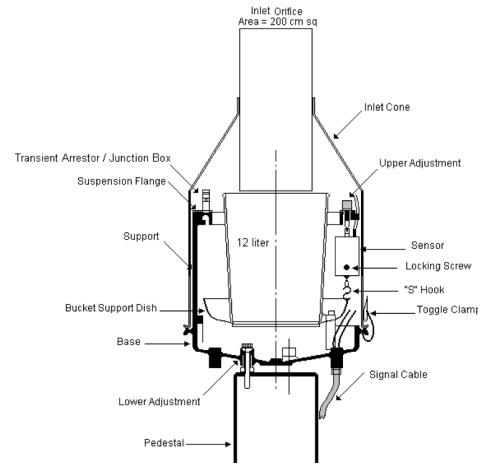
Since the winter season 2010/2011 Haukeliseter is equipped with several precipitation gauges. The wind shielded gauges are placed perpendicular to the main wind direction (E/W wind). The precipitation gauge protected by an octagonal double fence (Figure 3.1.2a) will be the reference to all surface accumulation measurements. The double fence creates an artificial calm wind and maximize the catch of precipitation, [Wolff et al., 2010, 2013, 2015]. The wind inside the double fence is measured to be not much higher than 5 m s^{-1} even if the winds outside exceed 20 m s^{-1} (occurred 26 December 2016). For now, it is presumed that the average undercatch inside a double fence is 20 % for wind speeds between 10 m s^{-1} and 20 m s^{-1} and 10 % for wind speeds under 9 m s^{-1} [Wolff, 2018].

Inside the double fence is a precipitation-weighing gauge Geonor T-200B3 [3-wire transducers, 1000 mm, Geonor Inc., 2015] with a Alter wind screen to reduce wind turbulence around the gauge. At Haukeliseter is the orifice height of the Geonor 4.5 m above the ground. This is due to an expected snow depth of 2 m to 3 m during a winter season and to reduce the likelihood of measuring drifting snow [Wolff et al., 2013, 2015].

A vertical cross section of the T-200B gauge is shown in Figure 3.1.2b. Precipitation particles fall through the 200 cm^2 orifice protected with a heated collar, into a cylindric bucket filled with frost protection. The bucket is placed on top of a Bucket Support Dish [Figure 3.1.2b, Geonor Inc., 2015]. This dish is connected with three wire sensors having an eigenfre-



(a)



(b)

Figure 3.1.2: a: Double fence and unprotected precipitation gauges at Haukeliseter, from Wolff et al. [2015]. The prevailing wind direction from east comes from the lower, left corner in the image and the west wind from the opposite site. b: Vertical cross section of T-200B precipitation gauge [Geonor Inc., 2015].

quency changing with the weight inside the bucket. A formula provided by [Geonor Inc. \[2015\]](#) calculates the amount of precipitation from the frequency of each sensor. The three sensors provide a reduction of an error in connection with an unlevel installation. Met-Norway will average value of all three sensors and provide it as hourly data at [eklima](#).

3.1.2 MRR - MICRO RAIN RADAR

Radars are very useful to observe the vertical of the atmosphere. The instrument is able to detect mesoscale features and makes it possible to see the vertical structure of storms [[Markowski and Richardson, 2011](#)].

The principle of radar measurements is based on an electromagnetic wave, which is emitted from the radar transmitter and interacts with the hydrometeors along the beam. A fraction of the pulse energy is reflected back to the receiver of the radar. The quantity of scattering depends on the shape and structure of the reflected particle. Vertical profiles of reflectivity give information about the diameter of the target object.

The Micro Rain Radar, in Figure 3.1.3, measures profiles of Doppler spectra [[METEK, 2010](#)]. The Doppler spectrum tells about the movement of the particle. The vertical pointing Doppler radar measures the energy that is returned from each interval and thus enabling the detection of the Doppler spectrum [[L'Ecuyer, 2017](#)]. The MRR measures at a frequency of 24 GHz, and has a temporal and spatial spatial resolution of 60 s and 100 m, respectively. The radar height range is from 100 m (because of ground clutter) to 3.000 m [[METEK, 2010](#)]. MRR radar reflectivity (Z) is transformed from $1 \text{ mm}^6/\text{m}^3$ to dBZ. The transformations is done with the following relationship;

$$Ze = 10 \log_{10} \left(\frac{Z}{1 \text{ mm}^6/\text{m}^3} \right) \quad [\text{dBZ}] \quad (3.1.1)$$



Figure 3.1.3: Micro Rain Radar.

A transformation to rainfall rates can be performed by the $Z-R$ (reflectivity - rainfall) relationship. The rainfall rate in each layer can be estimated by the use of typical fall speeds and the Marshall-Palmer particle size distribution for liquid particles [[Rinehart,](#)

Table 3.1.1: Typical reflectivity values, from [Doviak and Zrnic \[1993\]](#). The values are obtained from measurements, models and observations. The rainfall rate R is calculated with Equation (3.1.2).

	Ze [dBZ]	R [mm h ⁻¹]
Drizzle	<25	1.3
Rain	25 to 60	1.3 to 205.0
Snow		
dry, low density	<35	5.6
Crystal; dry, high density	<25	1.3
wet, melting	<45	23.7
Graupel		
dry	40 to 50	11.5 to 48.6
wet	40 to 55	11.5 to 99.9
Hail		
small; <2 cm, wet	50 to 60	48.6 to 205.0
large; >2 cm, wet	55 to 70	99.9 to 864.7
Rain & Hail	50 to 70	48.6 to 864.7

[2010](#)].

$$Z = 200R^{\frac{8}{5}} \quad [\text{mm}^6 \text{m}^{-3}]$$

$$R = \left(\frac{10^{\frac{Ze}{10}}}{200} \right)^{\frac{5}{8}} \quad [\text{mmh}^{-1}] \quad (3.1.2)$$

Table 3.1.1 represents the Z-R relationship if the Marshall-Palmer assumption (Equation (3.1.2)) is applied. Z-snowfall relationships are developed but are difficult to apply due to the variation of size and density of the particles [[L'Ecuyer, 2017](#)].

After the transformation to dBZ the reflectivity is averaged for every 200 m layer thickness, where only values above 300 m are taken. For instance, a reflectivity at 400 m represents the mean value of reflectivity between 300 m and 500 m.

3.1.3 PiP - PRECIPITATION IMAGING PACKAGE

The precipitation imaging package (PiP) is a modification of the Snowflake Video Imager presented by [Newman et al. \[2009\]](#). The video distrometer is a construct of a halogen flood lamp and a video system (Figure 3.1.4). The instrument determines the habit of snowflakes from images at a frequency of 60 Hz. Lamp and lens have a distance of approximately 3 m which follows a field of view: 32 mm by 24 mm.

In front of the halogen lamp is a frosted window, so that the background light is uniform over all time. A falling particle appears as a 2-D shadow in the video image. Particle size distribution (PSD) and fall speed of precipitation can be determined from the black and white images of the system. [Newman et al. \[2009\]](#) describes in detail the algorithm applied to the system to get information about the snow-particle habit.

Winds have almost no effect on the result of the video distrometer [[Newman et al., 2009](#)]. They also say, to reduce eventual wind effects, should the distrometer be oriented with regard to storm winds (optical axis perpendicular to mean wind). Was that the case for Haukeliseter (I'm just curious)???



Figure 3.1.4: Precipitation Imaging Package.

3.1.4 MASC - MULTI-ANGULAR SNOWFALL CAMERA

Instruments like the afore mentioned PiP has according to [Garrett et al. \[2012\]](#) coarser resolution and the determination of particle size can have larger errors. Hence, a new instrument was developed. The Multi-Angular Snowfall Camera (MASC) takes high-resolution images of hydrometeors in free fall and measures the fall-speed simultaneously.

The MASC consists of three cameras, three flashes, and two near-infrared sensors, pointing at a ring centre (Figure 3.1.5). A hydrometeor has to pass through the ring in a certain way to trigger the near-infrared sensors. At the same time the three cameras take a picture of the falling particle. Since the cameras take pictures from three different angles, the particles size, shape, and orientation can be specified from an algorithm applied to the image, described in [Garrett et al. \[2012\]](#). Furthermore, the form and heritage of the hydrometeor, such as collision-coalescence, riming, capture nucleation, or aggregation, can be determined. The near-infrared sensor, that is used to trigger the cameras and the lights quantifies the fall-speed of the hydrometeors, by measuring the time the particle needs to pass the distance between the upper and lower trigger.

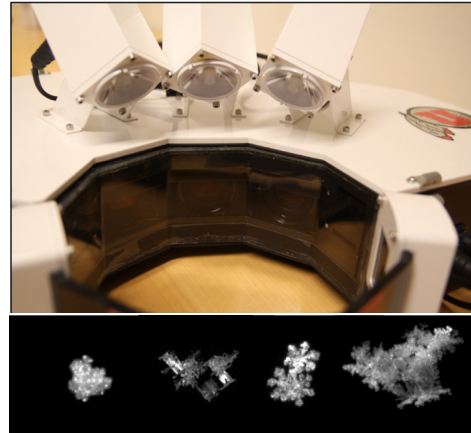


Figure 3.1.5: MASC and images taken by instrument. **Lower panel taken from Cooper et al. [2017] maybe we get one for Haukeli?**

3.2 OPTIMAL ESTIMATION RETRIEVAL ALGORITHM

Since 2006, with the launch of CloudSats Cloud Profiling Radar (CPR) a global estimation of snowfall can be done. Several studies, such as [Kulie and Bennartz \[2009\]](#) have shown that estimated snowfall values depend heavily upon assumed snowflake microphysical properties. [Wood et al. \[2015\]](#) showed that a refinement of the CloudSat snowfall retrieval algorithm can be performed by using snowflake models. This study was based on data from the Canadian CloudSat-CALIPSO Validation Project [C3VP, [Hudak et al., 2006](#)], where they concentrated on cold season clouds and precipitation.

In an attempt to reduce the non-uniqueness of the problem, [Wood et al. \[2015\]](#) used the a priori knowledge of snowfall microphysics and temperature (from ground-based observations) to refine the forward-model assumptions for the CloudSat snowfall retrieval scheme. Results from this scheme showed a good agreement with reported values observed at meteorological measurement sites.

Model estimates have proven, how useful the estimation retrieval can be to verify ground-based radar snowfall measurements [[Norin et al., 2015](#)]. Although the retrieval has obviously been improved the estimation algorithm, a priori guess can still lead to uncertainties in the retrievals of up to 140 % to 200 % [[Wood, 2011](#)].

[Cooper et al. \[2017\]](#) developed a technique to combine MRR, MASC, and PiP information into a common retrieval framework. Specifically, estimates of snowflake microphysical properties from the MRR are used as the a priori term in the optimal-estimation retrieval scheme. The usage of either MASC/PiP or MRR fall-speed can show which a priori guess in the retrieval gives the more accurate retrieved snowfall rate at the ground.

The difference between the retrieval and the snow gauge observations was –18 % when applied to data from Barrow, Alaska.

[Cooper et al. \[2017\]](#) also showed that the retrieval is sensitive to habit and fall speed. The installation of a MRR, MASC, and PIP should help to adjust the particle models for graupels and rimed particles which are often observed at Haukeliseter.

3.2.1 PRESENT SNOW

To achieve vertical profiles of snowfall from MRR different steps and assumptions are done in the here presented snowfall retrieval. From one of the lower levels, the snowfall rate at the surface can be estimated. The retrieval is only performed for profiles, which are likely to have observed snow, where most retrievals use rain. In previous studies relationships between reflectivity and snowfall have been developed. Even if the PSD of ice particles is known, different crystal shapes led to different results. Snow densities vary significantly from storm to storm, where small particles are still Rayleigh scattered, and larger particles non-Rayleigh scattered [[Gunn and East, 1954](#)].

To obtain the likelihood of present snow a reflectivity threshold of –15 dBZ is used. This threshold is similar to the one used in [Wood et al. \[2013b\]](#), where it states that light liquid precipitation is related to –10 dBZ [[Stephens and Wood, 2007](#)]. [Wood \[2011\]](#) compared

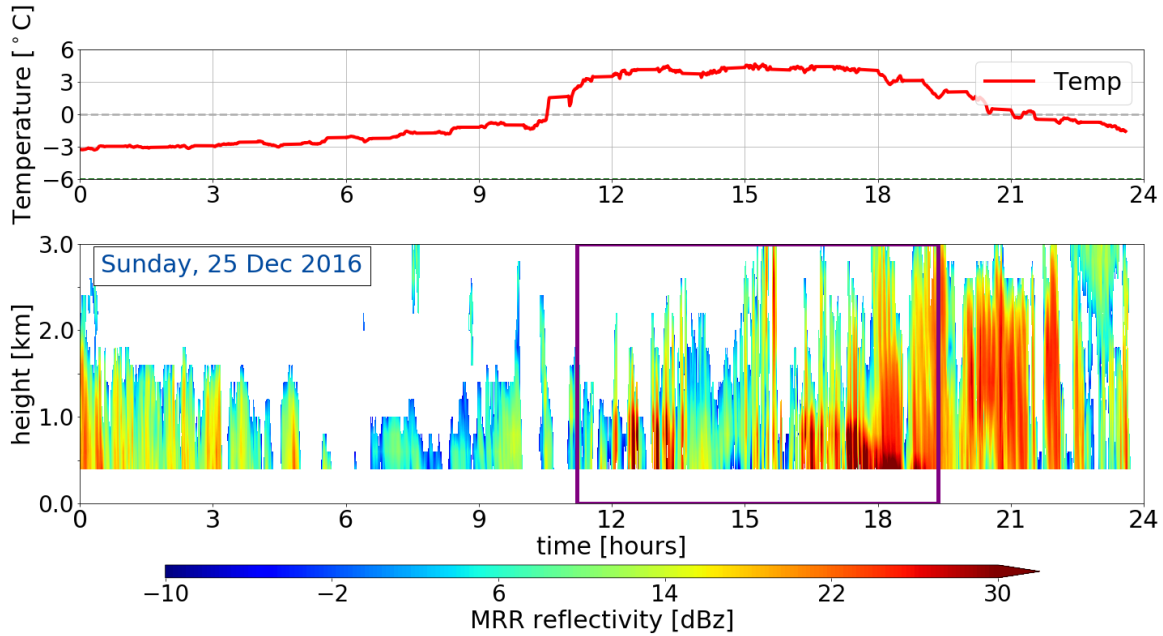


Figure 3.2.1: Shows the a priori temperature dependence within the optimal estimation retrieval for an all day precipitation event on 25 December 2016. The upper panel shows T_{ap} measured at the Haukeliseter site. The lower panel presents the reflectivity from the MRR in addition indicates the purple frame the time, where the MRR reflectivity was larger than -10 dBZ and surface temperatures less than 2°C

the reflectivity in the lowest bin and adjacent bin and found, that the reflectivity above -15 dBZ are not influenced by ground clutter.

The Haukeliseter measurement site is equipped with a weather mast, measuring the air temperature every minute at two meter height (compare Figure 3.2.1, upper panel). Since the MRR measures above 300 m and only temperature measurements at the surface exists, a priori temperature (T_a) is assumed to be similar to the observed near-surface air temperature. Using a moist adiabatic lapse rate of $dT/dz = 5 \text{ K km}^{-1}$ gives T_a in each layer. Assuming snow exists at temperature measurements up to a threshold of 2°C , validated by Liu G. [2008] who analysed present weather reports to find the distinction between liquid and solid precipitation.

The purple line in the lower panel of Figure 3.2.1 represents the time frame during 25 December 2016, where the MRR reflectivity is less than -15 dBZ , and a priori temperature passes the 2°C limit at the surface.

3.2.2 SIZE DISTRIBUTION

To determine the snowfall rate at the surface an exponential particle size distribution (PSD) is needed.

$$n(r) = N_0 \exp(-\lambda r) \quad [\text{m}^{-3} \text{ mm}^{-1}] \quad (3.2.1)$$

where λ represents the PSD slope parameter and N_0 the number density. r is the particle maximum dimension evaluated from the 2D-scattering model for branched 6-arm spatial particles with porosities for reflectivity measurements at 24 GHz (see Appendix A).

Since T_a varies with a moist adiabatic lapse rate in each layer bin the slope parameter and the number density in Equation (3.2.1) are changing too. [Wood \[2011\]](#) showed a linear fit between $\log(\lambda)$ and the a priori temperature, respectively $\log(N_0)$ and the a priori temperature. Using T_a in °C for each layer bin the following logarithmic assumption is used, to define the slope parameter and the number density.

$$\log(\lambda) = -0.03053 \cdot T_{ap} - 0.08258 \quad [\log(\text{mm}^{-1})] \quad (3.2.2)$$

$$\log(N_0) = -0.07193 \cdot T_{ap} + 2.665 \quad [\log(\text{m}^{-3} \text{ mm}^{-1})] \quad (3.2.3)$$

To achieve the state vector \mathbf{x} of unknown microphysical properties, the log-transformed values are taken.

$$\mathbf{x} = \begin{bmatrix} \log(\lambda)_0 \\ \vdots \\ \log(\lambda)_{\text{nlayer}} \\ \log(N_0)_0 \\ \vdots \\ \log(N_0)_{\text{nlayer}} \end{bmatrix} \quad \text{nlayer} = 14 \quad (3.2.4)$$

The log-transformed equation is useful, since the results from C3VP were similar to other observations. The study showed, that N_0 ranges over several order of magnitude as well as λ was non-Gaussian for the snow events [Wood \[2011\]](#).

3.2.3 SNOWFALL RETRIEVAL SCHEME

The optimal estimation method is based on Gaussian statistics. Minimizing the scalar cost function, Φ for the snowfall properties, \mathbf{x} . The cost function weights the difference

between the observed reflectivity and the simulated measurements as well as the difference between the estimated and a priori guess.

Scalar cost function:

$$\begin{aligned}\Phi(\mathbf{x}, y, a) = & (y - F(\mathbf{x}))^T \mathbf{S}_y^{-1} (y - F(\mathbf{x})) \\ & + (\mathbf{x} - a)^T \mathbf{S}_a^{-1} (\mathbf{x} - a)\end{aligned}\quad (3.2.5)$$

where, \mathbf{x} , vector of retrieved snowfall properties (Equation (3.2.4)); y , vector of observation (MRR reflectivity); a , vector of the a priori guess (temperature dependent); \mathbf{S}_a , a priori error covariance matrix; \mathbf{S}_y , measurement error covariance matrix. The forward model $F(\mathbf{x})$, presented in Section 3.2.4 relates unknown snowfall parameters \mathbf{x} to radar observations y and approximates the true physical state between them [Cooper et al., 2017, Wood et al., 2014].

\mathbf{S}_a links the uncertainties of the PSD information and the surface temperature differences. The diagonal matrix elements in \mathbf{S}_a are equal to 0.133 and 0.95 for the particle slope parameter and the number density, respectively as from Eq. 7.35 and 7.36 in Wood [2011]. \mathbf{S}_y characterises the the uncertainties associated with the measurements and the error in the forward model. This study uses for the diagonal matrix elements 2.5² UNIT! based on the study from CITATION. BECAUSE.

I don't understand the next steps and if it is still the same \mathbf{x} ?

At convergence is the error covariance of the retrieved state vector \mathbf{S}_x

$$\mathbf{S}_x = \left(\mathbf{S}_a^{-1} + \mathbf{K}^T \mathbf{S}_y^{-1} \mathbf{K} \right)^{-1} \quad (3.2.6)$$

which follows for \mathbf{x}

$$\mathbf{x} = \underbrace{\left(\mathbf{S}_a^{-1} + \mathbf{K}^T \mathbf{S}_y^{-1} \mathbf{K} \right)^{-1}}_{\mathbf{S}_x} \left(\mathbf{S}_a^{-1} a + \mathbf{K}^T \mathbf{S}_y^{-1} (y - F(\mathbf{x}) + \mathbf{K}x) \right) \quad (3.2.7)$$

The Jacobian matrix, \mathbf{K} , represents the sensitivity matrix of the perturbed result of the forward model. The true state \mathbf{x} is perturbed by $\pm 0.2\%$ and thus \mathbf{K} represents the relation between simulated values to the true state. Why are we perturbing it?

$$\mathbf{K}(\mathbf{x}) = \frac{\partial y}{\partial \mathbf{x}} = \begin{bmatrix} \frac{\partial y_0}{\partial \mathbf{x}_0} & \frac{\partial y_0}{\partial \mathbf{x}_1} & \cdots & \frac{\partial y_0}{\partial \mathbf{x}_{2 \times \text{nlayer}}} \\ \vdots & \vdots & \ddots & \vdots \\ \frac{\partial y_{\text{nlayer}}}{\partial \mathbf{x}_0} & \frac{\partial y_{\text{nlayer}}}{\partial \mathbf{x}_1} & \cdots & \frac{\partial y_{\text{nlayer}}}{\partial \mathbf{x}_{2 \times \text{nlayer}}} \end{bmatrix} \quad (3.2.8)$$

Usually, is \mathbf{K} not diagonal [Wood, 2011], hence it is a mix of the true state and the a priori guess and the influence from them can be estimated. The closer \mathbf{K} is diagonal, the more is \mathbf{x} determined by the real observed and a priori values. If the limit of the partial derivative is close to unity, the retrieved value \mathbf{x} is its true state [Wood, 2011].

mmmh? What exactly are we doing here? Test the if convergent:

$$\hat{x} = (\mathbf{x} - F(\mathbf{x}))^T \mathbf{S}_x^{-1} (\mathbf{x} - F(\mathbf{x})) \quad (3.2.9)$$

only if \hat{x} is smaller than 2 it is a 'good' retrieval.

To test the result of \mathbf{x} a χ^2 test is performed at the convergence of \mathbf{S}_x .

$$\begin{aligned} \chi^2 = & (F(\mathbf{x}) - y)^T \mathbf{S}_y^{-1} (F(\mathbf{x}) - y)^T \\ & + (\mathbf{x} - a)^T \mathbf{S}_a^{-1} (\mathbf{x} - a). \end{aligned} \quad (3.2.10)$$

The first term in Equation (3.2.10) measures the part of χ^2 related to the noise of the forward model, and the second part the relation to the state vector. Thus the second term describes the accuracy of the quantities within the reflectivity and temperature measurements [Rodgers, 2000]. Furthermore, are the error contribution from the reflectivity measurement uncertainty, \mathbf{S}_{y_e} , and the uncertainty of the a priori values, \mathbf{S}_{a_e} estimated. **Where comes this formulas from? Is the \mathbf{D}_y the \mathbf{K}_b in Eq. 15 in Wood et al. [2013a]? How to interpret?**

$$\mathbf{D}_y = \mathbf{S}_x \mathbf{K}^T \mathbf{S}_y^{-1} \quad \mathbf{S}_{y_e} = \mathbf{D}_y \mathbf{S}_y \mathbf{D}_y^T \quad (3.2.11)$$

$$\mathbf{D}_a = \mathbf{S}_x \mathbf{S}_a^{-1} \quad \mathbf{S}_{a_e} = \mathbf{D}_a \mathbf{S}_a \quad (3.2.12)$$

The diagonal of \mathbf{S}_{y_e} or \mathbf{S}_{a_e} is a first estimate of the retrieval noise related to the observations [Rodgers, 2000]. Uncertainties in \mathbf{S}_{a_e} occur because of the variability in T_a and similar for \mathbf{S}_{y_e} due to measurement errors from the MRR.

3.2.4 FORWARD MODEL

Forward model defines a relationship between the radar observations and the retrieved state vector \mathbf{x} . It is difficult to find the properties of the atmosphere by using observations due to unknown parameters influencing the measurement.

[Stephens \[1994\]](#) described the forward problem in the manner that a Dragon represents the known source, observations Figure 3.2.2. The amount of received radiation lost during the transmittance to the sensor is unknown, the Tracks in Figure 3.2.2. The forward model will help to find simulated observations before the attenuation took place and give information about the tracks of the dragon.

The knowledge about the a priori parameters and related covariances, as well as \mathbf{x} , are used to minimize Equation (3.2.5). The values of \mathbf{x} are found by Newtonian iteration [[Wood et al., 2014](#), Eq. 5].

The snow water content in each layer is estimated from the knowledge of the snow particle mass-dimension relationship in Appendix A, and a PSD related to slope parameter and number density (Equations (3.2.1–3)).

$$\text{SWC} = \int_{r_{min}}^{r_{max}} m(r) n(r) dr \quad [\text{gm}^{-3}] \quad (3.2.13)$$

To achieve a relationship between the reflectivity and the snowfall amount one needs to account for attenuation in the atmosphere. Using the previously calculated PSD (Equation (3.2.1)) the backscattering cross-section σ_{bk} , one can estimate the reflectivity for Rayleigh approximated, singly-scattered non-attenuated ice particles [[Kulie and Bentartz, 2009](#), [L'Ecuyer and Stephens, 2002](#), [Wood et al., 2015](#)]. The Rayleigh approximation assumes, that $2\pi r/\lambda \ll 1$, where λ the wavelength of incident radiation.

$$\begin{aligned} \eta_{bk} &= \int_{r_{min}}^{r_{max}} n(r) \sigma_{bk} dr \quad [\text{m}^{-1}] \\ Ze^{ss,na} &= \frac{\Lambda^4}{\|K_w\|^2 \pi^5} \eta_{bk} \quad [\text{mm}^6 \text{m}^{-3}] \end{aligned} \quad (3.2.14)$$

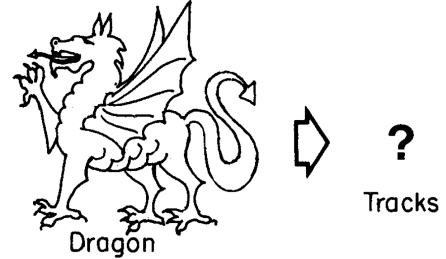


Figure 3.2.2: Relationship between measurements (dragon) and the unknown parameter of interest (tracks) [[Stephens, 1994](#)].

where, Λ is the wavelength of the radar; $\|K_w\|^2$ is the complex refractive index of water and varies between 0.91 and 0.93 for wavelength between 0.01 m and 0.10 m and is independent of temperature. It also exists a complex refractive index for ice $\|K_i\|^2$, which is 0.18. This is valid for a density of 0.917 g cm^{-3} and is independent of temperature and of wavelength in the microwave region [Doviak and Zrnic, 1993]. In this work $\|K_w\|^2 = 0.93$ is chosen, BECAUSE???

The singly-scattered reflectivity has to be corrected for attenuation in the layers above the actual layer. According to Beer's law is in a homogeneous medium one way transmission assumed.

$$\frac{I_\lambda}{I_{\lambda_0}} = \exp \left[- \int_0^s \beta_{ext} ds' \right] \quad (3.2.15)$$

where s is the path length through the medium. The transmissivity $I_\lambda / I_{\lambda_0}$ is the relation of survived radiation through extinction in the atmosphere with the snow extinction coefficient β_{ext}

$$\beta_{ext} = \int_{r_{min}}^{r_{max}} n(r) \sigma_{ext} dr \quad [\text{m}^{-1}] \quad (3.2.16)$$

The extinction coefficient is the sum of absorption and scattering in the atmosphere followed from the extinction cross-section $\sigma_{ext} = \sigma_{abs} + \sigma_{scat}$, [Lamb and Verlinde, 2011, Lohmann et al., 2016]. [Eq. 12.1 and more Lohmann et al., 2016]

Following Equations (3.2.14–16) the singly-scattered attenuated reflectivity $Ze^{ss,a}$ is

$$Ze^{ss,a} = Ze^{ss,na} \cdot \frac{I_\lambda}{I_{\lambda_0}} \quad [\text{mm}^6 \text{m}^{-3}] \quad (3.2.17)$$

That follows with the use of radiative transfer equations for the simulated reflectivity from the forward model, $F(\mathbf{x})$ in Equation (3.2.5), after the transformation with Equation (3.1.1)

$$F(\mathbf{x}) = \begin{bmatrix} Ze_1^{ss,a} \\ \vdots \\ Ze_{nlayer}^{ss,a} \end{bmatrix} \quad [\text{dBZ}] \quad (3.2.18)$$

- not really using the following - What to do with it?
- total number concentration

$$n_{tot} = \int_{r_{min}}^{r_{max}} n(r) dr \quad [\text{m}^{-3}]$$

- ... ???

3.2.5 SNOWFALL RATE AT THE SURFACE

To achieve snowfall rates at the surface, the snow water content (Equation (3.2.13)) has to be transformed. The use of an assumed particle fall speed of $V = 0.85 \text{ m s}^{-1}$ and the retrieved SWC (Equation (3.2.13)) gives the snow mass flux $J_{snow} = \text{SWC} \cdot V$ in $[\text{kg m}^{-2} \text{ s}^{-1}]$. Why did we use this fall speed? Where does this assumption come from? Similar as Cooper et al. [2017] Eq. 4? To compare retrieved snow fall rates to double fence measurements and the forecast model output, the precipitation amount at the surface is calculated.

$$P = J_{snow} \times 10^{-3} \cdot (3600 \text{ s} \cdot 24) \quad [\text{mm d}^{-1}] \quad (3.2.19)$$

The precipitation amount at the surface, presented in Chapter 5, are taken to be equal to the values at the snow layer in 800 m. The use of the values at 800 m is due to the small increase of reflectivity (ground clutter) in the bottom layers and would follow more observed snow.

- Not sure what to do with this!
- The error from the retrieved state vector \mathbf{x} is calculated

$$\pm \mathbf{S}_{x_{err}} = \mathbf{x} \pm \mathbf{S}_x$$

$$equiv_{err} = \frac{1}{2} \left(\frac{|SWC(-\mathbf{S}_{x_{err}}) - SWC(+\mathbf{S}_{x_{err}})|}{SWC(-\mathbf{S}_{x_{err}})} + \frac{|SWC(-\mathbf{S}_{x_{err}}) - SWC(-\mathbf{S}_{x_{err}})|}{SWC(-\mathbf{S}_{x_{err}})} \right)$$

3.3 NUMERICAL FORECAST MODEL

MEPS (MetCoOp Ensemble Prediction System) was newly operational at Met-Norway when the extreme weather occurred in Norway. Comparing model data with actual observations helps to verify the agreement between model prediction and ground based measurements.

AROME-MetCoOp was operational from March 2014 until November 2016, when it was replaced with an ensemble prediction system (EPS) based on AROME-MetCoOp. MEPS is used as weather forecast at the Norwegian Meteorological Institute, the Swedish Meteorological and Hydrological Institute (SMHI) and the Finnish Meteorological Institute (FMI), [Køltzow, 2017, Müller et al., 2017].

3.3.1 AROME - METCOOP

In principle, MEPS is a short-term weather forecast of 66 h with 10 ensemble member and a horizontal resolution of 2.5 km and 65 vertical levels. One of the members is the deterministic forecast where the other nine present the perturbed state of the deterministic forecast. The initialisation of each member is performed at 0 UTC, 6 UTC, 12 UTC and 18 UTC [MetCoOp Wiki, 2017].

The orange frame in Figure 1.1.1 shows the MEPS model domain as it was operational for December 2016. It covers the Nordic Countries including open water such as the Atlantic Ocean, the North and the Baltic Sea.

The centre of the model is approximately at 63.5° N, 15° E. The horizontal grid points are projected on a Lambert projection to receive the same area size of each grid cell. The outer, parent grid is the ECMWF-IFS model (European Centre for Medium-Range Weather Forecasts Integrated Forecasting System) with a horizontal resolution of 9 km [Homleid and Tveter, 2016]. The ECMWF-IFS forecasts are used 6 h prior to the actual cycle in MEPS. Vertical hybrid coordinates are terrain-following and are mass-based, [Müller et al., 2017]. How the vertical hybrid coordinates were transformed into layer thickness or height is described in Section 3.4.1. Furthermore, MEPS underlies non-hydrostatic dynamics, MetCoOp Wiki [2017].

The representation of snow is covered by a modification of the three-class ice parametrization (ICE3) scheme. Where liquid-phase processes are separated from slow ice-phase processes and described in Section 3.3.2. To model the snow cover an one-layer atmosphere model scheme is implemented. This includes three variables such as: snow water equivalent (SWE), snow density, and snow albedo [Müller et al., 2017].

As synoptic observations are included in the model the snow-depth predictions underlay a special performance. Observations of snow-depth are only available at 6 UTC and 18 UTC, therefore is the snow analysis only performed twice daily [Homleid and Tveter, 2016, Müller et al., 2017].

3.3.2 MESO-NH AND THE ICE3 SCHEME

The physical parametrization within AROME is based on the French research communities' mesoscale non-hydrostatic atmosphere model (Meso-NH). The microphysical scheme in

the Meso-NH atmospheric simulation system is based on the ICE3 scheme. The purpose of the scheme is to model as correctly as possible the ice phase in the atmosphere and it is assumed that no rain formation occurs at temperatures below 0 °C [Pinty and Jabouille, 1998]. McCumber et al. [1991] concluded from their case study, that at least three different ice categories are necessary to cover most precipitation but that applications might be case specific. According the Meteo France [2009] documentation must the ice phase microphysical scheme include:

\mathbf{r}_i : pristine ice phase from heterogeneous nucleation

\mathbf{r}_s : snowflake type from lightly rimed large ice crystals or dry clusters, and

\mathbf{r}_g : heavily rimed crystals, such as graupel, frozen drops or hail

Within the ICE3 scheme no distinction between hail and graupel exists and therefore is the physical discrimination in the growth mode of graupel and hail neglected.

To achieve snow water content within MEPS the total number concentration, slope parameter, mass diameter and the particle size distribution have to be determined. According to Caniaux et al. [1994] follows the particle size distribution the Marshall-Palmer distribution similar to Equation (3.2.1). The goal is to use a varying number density N_0 dependent on the ice category. The study has shown that N_0 can be assumed with

$$N_0 = C\lambda^x \quad (3.3.1)$$

$$\log_{10} C = -3.55x + 3.89$$

where C and x depend on the ice category and represent the relation between each other in Equation (3.3.1).

The ice water content for primary ice, snowflakes and rimed crystals is then be assumed to be similar to Equation (3.2.13), but the integration limits range from zero to infinity and mass, and particle size distribution are dependent on the diameter of the particle. The mass diameter and particle size distribution (Equations (3.3.2) and (3.3.3)) are represented depending on the ice category shown in Table 3.3.1

$$m(D) = aD^b \quad (3.3.2)$$

$$n(D) = N_0 g(D) \quad (3.3.3)$$

and $g(D)$ to be the generalised Gamma function

$$g(D) = \frac{\alpha}{\Gamma(\nu)} \lambda^{\alpha\nu} D^{\alpha\nu-1} \exp(-(\lambda D)^\alpha) \quad (3.3.4)$$

with α, ν the shape and tail dispersion parameters and $\Gamma(\nu)$ the gamma function.

After following the above equations including Equation (3.2.13) the slope parameter λ can be generated.

$$\lambda = \left(\frac{\text{SWC}}{aCG(b)} \right)^{\frac{1}{x-b}} \quad (3.3.5)$$

What is $G(b)$?

Table 3.3.1: Characterization parameters fro primary ice (r_i), snowflakes (r_s) and rimed crystals (r_g). Values are based on the references in [Meteo France \[2009\]](#) and in [Pinty and Jabouille \[1998\]](#).

	r_i	r_s	r_g
α, ν	3.3	1.1	1.1
a	0.82	0.02	196
b	2.5	1.9	2.8
c	800	5.1	124
d	1.0	0.27	0.66
C		5	5×10^5
x		1	-0.5

[Meteo France \[2009\]](#) documentation suggests to start the microphysics in the ICE3 scheme with 'slow' processes such as homegeneous and heteorogeneous nucleation (HON, HEN), vapour deposition of snow and graupel particles (DEP), aggregation (AGG) and autoconversion (AUT), for ice processes right side in Figure 3.3.1. The second step is to initiate the warm processes left side in Figure 3.3.1. Then include the aggregation and conversion-melting (CVM) for snowflakes and contact freezing of raindrops (CFR). Add AGG and melting for graupel (MLT), and then the melting from pristine ice and the Bergeron-Findeisen (BER) process and lastly the sedimentation terms.

Figure 3.3.1 shows the summary of the microphysical processes for mixed phase clouds.

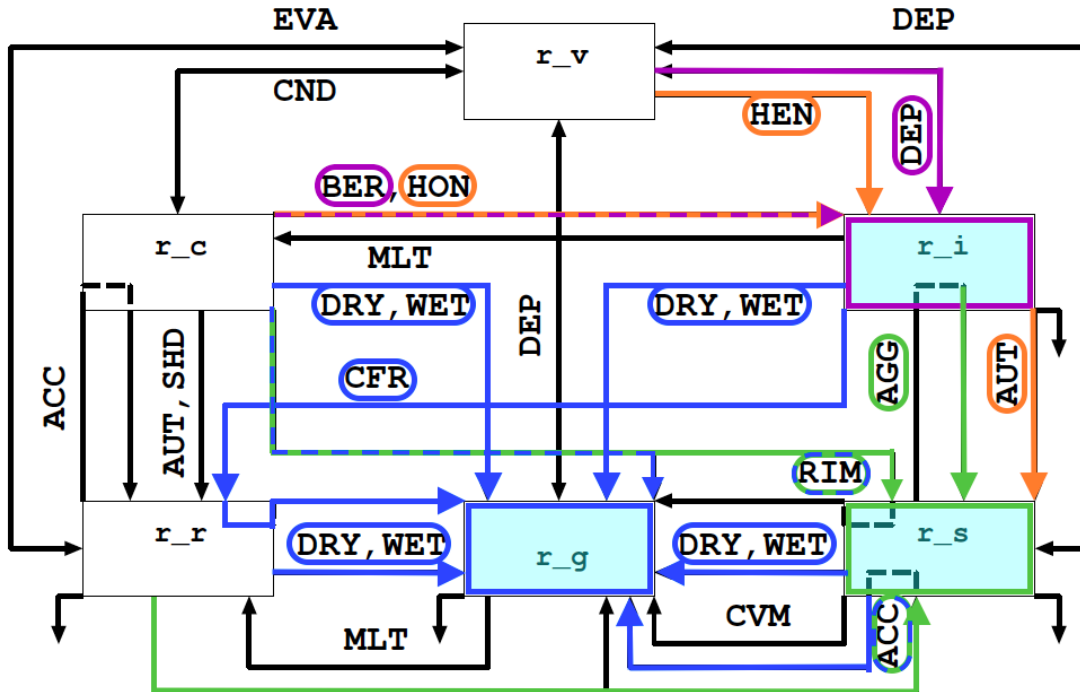


Figure 3.3.1: Microphysical processes for mixed phase clouds in the ICE3 scheme adapted from Meteo France [2009]. In orange the initiation processes for primary ice r_i and snowflakes r_s . The growing processes of r_i is shown in purple and for r_s in green. Graupel particles, r_g , grow from existent particles and the processes are shown in blue.

The study focuses mostly on solid precipitation particles and therefore only the initiation and growth of pristine ice crystals r_i , snowflakes r_s , and rimed crystals r_g is presented. Following Pinty and Jabouille [1998] and Figure 3.3.1 it can be seen how AROME performs the ice production. Orange lines in Figure 3.3.1 show the initiation of pristine ice crystals and snowflakes. In purple the growing mechanisms of r_i (BER,DEP). Green lines demonstrate the expansion of the snowflakes (RIM, AGG, ACC). Graupel (r_g) forms as an effect of heavy riming (RIM), by collision of larger raindrops with snowflakes (ACC), by WET/DRY growth or by contact freezing of raindrops (CFR). All graupel growth processes are indicated by blue lines in Figure 3.3.1, were hail formation is included.

3.3.3 ADJUSTMENT OF ICE3 INSIDE MEPS

Since the ICE3 scheme showed some weaknesses for the winter month, Müller et al. [2017] introduced some modifications. During cold conditions the ICE3-scheme showed too low temperature at two meter, too much ice fog and all year long was the occurrence of cirrus overestimated. After implementing the modifications described in Müller et al. [2017] the two meter temperature bias was reduced as well as an improvement of low-level clouds was shown. An negative aspect of these adjustments was that the occurrence of fog increased, but it can be compensated if no changes are done to the microphysics.

3.4 DATA PROCESSING

The previous Sections 3.2 and 3.3 represented the details on retrieving snowfall amounts from the optimal estimation retrieval and the forecast model outputs. The following section will describe how the different variables where processed to achieve a comparison between the retrieved values and the forecast model output.

3.4.1 LAYER THICKNESS IN MEPS

To compare the measurements from the surface with the MEPS data, the closest grid point is used to Haukeliseter.

MEPS has a vertical resolution in hybrid sigma pressure coordinates, were one is at the surface and decreases with height. To calculate the actual vertical pressure in Pa, a formula is provided in the OPeNDAP Dataset of `meps_full_2_5km_*.nc` by the Norwegian Meteorological Institute [2016].

$$p(n, k, j, i) = a_p(k) + b(k) \cdot p_s(n, j, i) \quad [\text{Pa}]. \quad (3.4.1)$$

p_s is the surface air pressure in Pa, and information about the variables a_p , b are not given from the access form. **On what is this based on?**

The next step was to convert pressure-levels into actual heights by the use of the hypsometric equation. Here, the air temperature in model levels is used to calculate the mean

temperature of each layer.

$$\bar{T} = \frac{\int_{p_1}^{p_2} T \partial \ln p}{\int_{p_1}^{p_2} \partial \ln p} \quad [\text{K}] \quad (3.4.2)$$

For the numerical integration, the Simpson rule was used, which is a build-in function in Python.

[Martin \[2006\]](#) presents steps of differentiating the hypsometric equation by using the virtual air temperature. But when the atmospheric mixing ratio is large, will the virtual temperature only be 1 % larger than the actual air temperature. Since the error is little calculations are done with the provided air temperature in model levels.

The thickness, Δz , of each layer is then be found by using the hypsometric equation from [Martin \[2006\]](#) and the previously calculated mean temperature (Equation (3.4.2)):

$$\Delta z = z_2 - z_1 = \frac{R_d \bar{T}}{g} \ln \left(\frac{p_1}{p_2} \right) \quad [\text{m}] \quad (3.4.3)$$

where R_d is gas constant for dry air with a value of $287 \text{ J kg}^{-1} \text{ K}^{-1}$, standard gravity $g = 9.81 \text{ m s}^{-2}$. p_1 and p_2 are the pressure levels at lower and higher levels, respectively ($p_2 < p_1$). To gain the respective height of each pressure layer, Δz is summed.

3.4.2 SNOW WATER CONTENT

To get a valid comparison between the SWC from the optimal estimation retrieval and the results from MEPS, the SWC is averaged over each hour. Taking the model initialisation of MEPS at 0 UTC the model produces forecast values at 0, 1, 2, ..., 22, 23, ..., 66 UTC. To approach hourly mean values from the retrieval SWC an average over 30 min prior and 29 min after each full hour is performed. This leads to a match of the average value at the same time as from MEPS.

Since MEPS has a higher vertical resolution than the optimal estimation snowfall retrieval each vertical profile of SWC is averaged every 200 m. To accomplish the same vertical resolution only values above 100 m are used to start at the same range height as given from the MRR (Section 3.1.2).

Within the output from MEPS snow water content does not exist for each model layer.

Hence the calculation of the SWC is performed by using the three solid precipitation categories given in MEPS. Namely the mixing ratio of snowfall (r_s), graupelfall (r_g) and the atmosphere cloud ice content (r_i). The mixing ratios are represented in kg kg^{-1} and a transformation to gm^{-3} is performed. Densities in each model level (ρ_{ml}) are calculated and then multiplied with the sum of the solid precipitation mixing ratio.

$$\rho_{ml} = \frac{p_{ml}}{R_d T} \quad [\text{kg m}^{-3}] \quad (3.4.4)$$

$$SWC_{ml} = \rho_{ml} \cdot (r_s + r_g + r_i)_{ml} \cdot 10^6 \quad [\text{gm}^{-3}]. \quad (3.4.5)$$

3.4.3 SNOW WATER PATH

The snow water path (SWP) is the vertically integrated value of the averaged SWC (Equations (3.2.13) and (3.4.5)), where the numerical Simpson's integration is applied.

$$\int_{h_0}^{h_1=3000\text{m}} SWC(h) dh \approx \frac{h_1 - h_0}{6} \left[SWC(h_0) + SWC(h_1) + 4SWC\left(\frac{h_0 + h_1}{2}\right) \right] \quad [\text{gm}^{-2}] \quad (3.4.6)$$

The snow water path is a measure of the weight of ice particles per unit area. It indicates the total amount of ice in the atmosphere.

3.4.4 DEW POINT TEMPERATURE FOR SKEW-T LOG-P DIAGRAM

The Python module pyMeteo is used to calculate the dew point temperature of each ensemble member to study the stability of the atmosphere (<https://pythonhosted.org/pymeteo/>, last visited: 25.01.2018). The additional package thermo.py is able to calculate the dew point temperature if the pressure and the specific humidity in each level are known.

$$e_l = \ln\left(\frac{\frac{q_v}{\epsilon} \cdot \frac{p}{100}}{1 + \frac{q_v}{\epsilon}}\right) \quad (3.4.7)$$

$$T_d = 273.15 + \frac{243.5 \cdot e_l - 440.8}{19.48 - e_l} \quad [\text{K}] \quad (3.4.8)$$

where, q_v is the specific humidity, p pressure in [Pa], $\epsilon = R_d/R_v = 0.622$ with R_v gas constant for water vapour.

CHAPTER 4: ANALYSIS OF THE CHRISTMAS STORM 2016

The overleaf file from the Synoptic weather situation is here:

<https://www.overleaf.com/13946126xwbhxrcwbyd>

This extreme weather event is chosen since MEPS just became operational and in addition surface snow instruments were installed to profile the vertical at Haukeliseter. Preliminary test showed the overestimation of snow accumulation by MEPS compared to the measurements at the ground. Furthermore, was changed the phase between the precipitation.

The next sections will give a definition of an extreme weather, a description of the different weather maps, and a synoptic interpretation of the storm and why mixed phase precipitation was observed at Haukeliseter.

Before the analysis each weather maps' purpose will be presented to understand the connections between them. For this, the ECMWF ...blabla product... so many grid degree ... is processed.

4.1 EXTREME WEATHER

'Extreme weather' is a meteorological term, associated with the extent of a weather type. The Norwegian Meteorological Institute declares an extreme event, if strong winds, large amounts of precipitation and large temperature changes are expected before the event occurs. As well as a large avalanche risk is present and coastal areas are influenced by extremely high-water levels. All this occurred during the Christmas storm [Olsen and

Granerød, 2017].

Generally, an event is divided into four phases that it can be called extreme [Pedersen and Rommetveit, 2013].

Phase A: *Increased monitoring before the possible extreme weather.* The meteorologists give special attention to the weather situation. At this point it is not certain, that there will be an extreme weather event.

Phase B: *Short-term forecasts.* It is decided, that there will be an extreme event. The forecasts are more detailed and updates will be published at least every six hours. The event will get a name.

Phase C: *The extreme weather is in progress.* The meteorologists send out weather announcements at least every six hours.

Phase D: *The extreme weather event is over. Clean-up and repairs are in progress.* When the extreme weather is over the public is notified and information about the upcoming weather and clearing work is given.

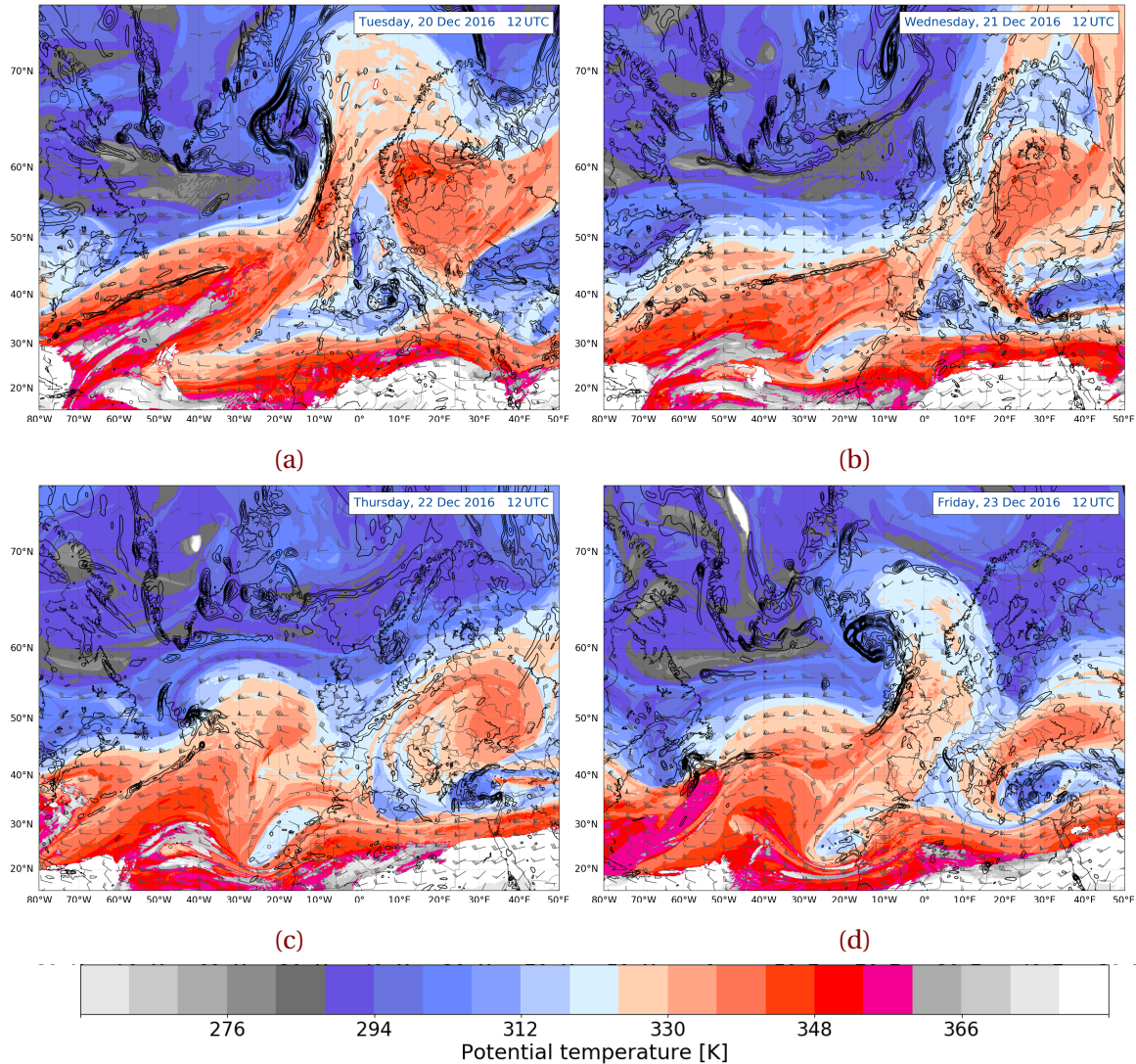
4.2 DYNAMIC TROPOPAUSE MAP

The dynamic tropopause map (DT), shown in Figure 4.2.1 presents the potential temperature distribution at the tropopause. Colder tropopause is associated with colder colours and vice versa warmer tropopause with warmer colours (shading according to the colorbar). Therefore, a warmer tropopause indicates an elevation of the atmospheric column.

The gradient at the 2 PVU (1 PV unit = $10^{-6} \text{ m}^2 \text{ s}^{-1} \text{ K kg}^{-1}$; Hoskins et al. [1985]) surface, between the cold and warm area indicates the thermal wind. There is a slope between the cold and warm surfaces increasing towards the warmer column averaged temperature. An increased slope means also an increased pressure gradient force with increasing height and therefore an increase in geostrophic wind. This means, that there exists a vertical wind shear. From this, the mid-latitude jet stream can be pointed out. **do I need to present the equation of thermal wind?** Wind barbs in m s^{-1} indicate the direction of the wind flow, which is generally from west to east in the mid-latitudes.

The 925–850 hPa layer-averaged surface relative vorticity is shown in black contours, every $0.5 \times 10^{-4} \text{ s}^{-1}$. It represents the rotation of a fluid. **Does the relative vorticity need more explanation?**

Along the Rossby-Wave-Guide, troughs and ridges are seen which can be combined with the surface relative vorticity to understand the vertical dynamic interaction in the atmosphere. In case of a westward tilt between the surface cyclone and an upper level through an intensification of the surface cyclone is more likely to occur.



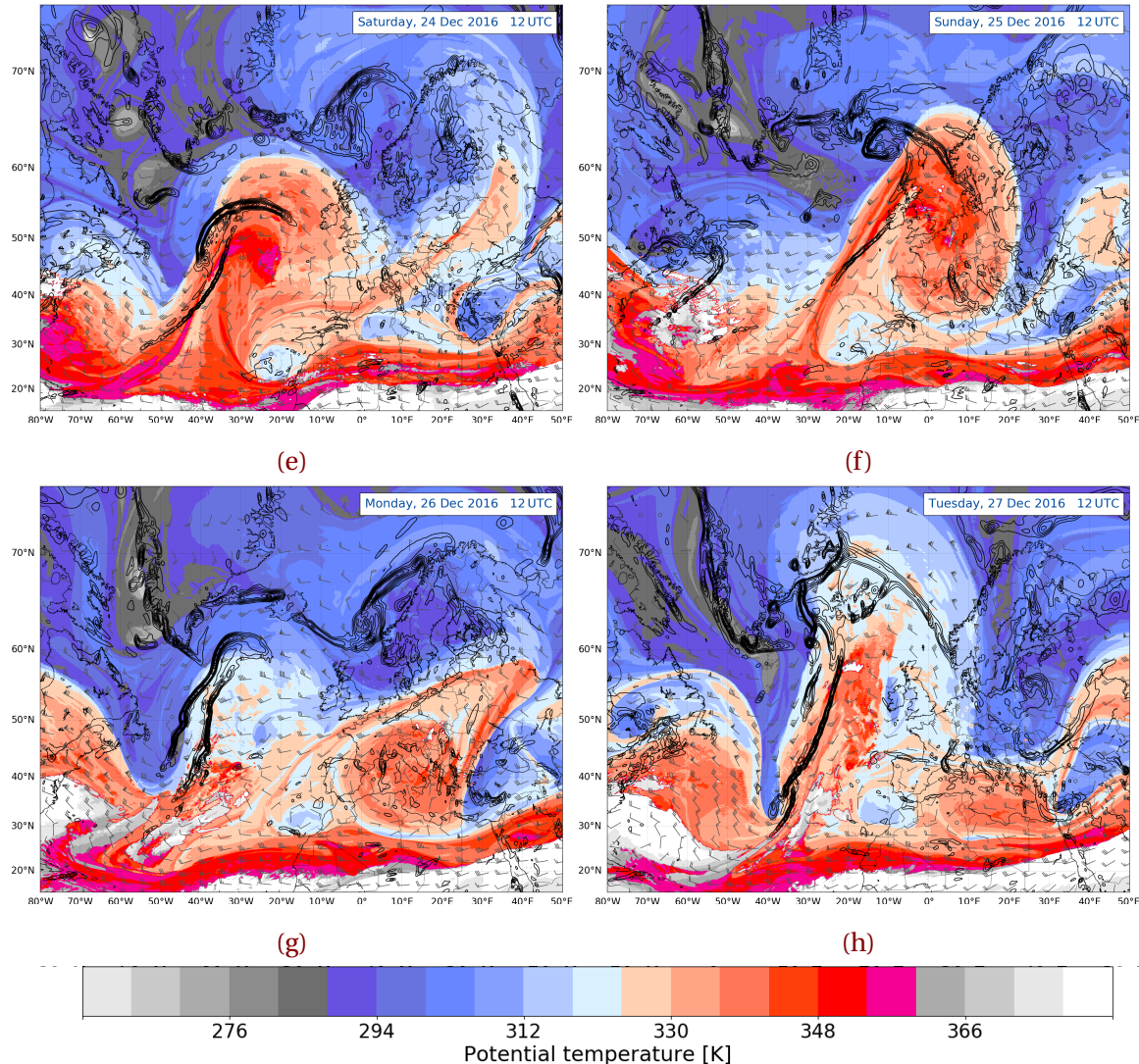
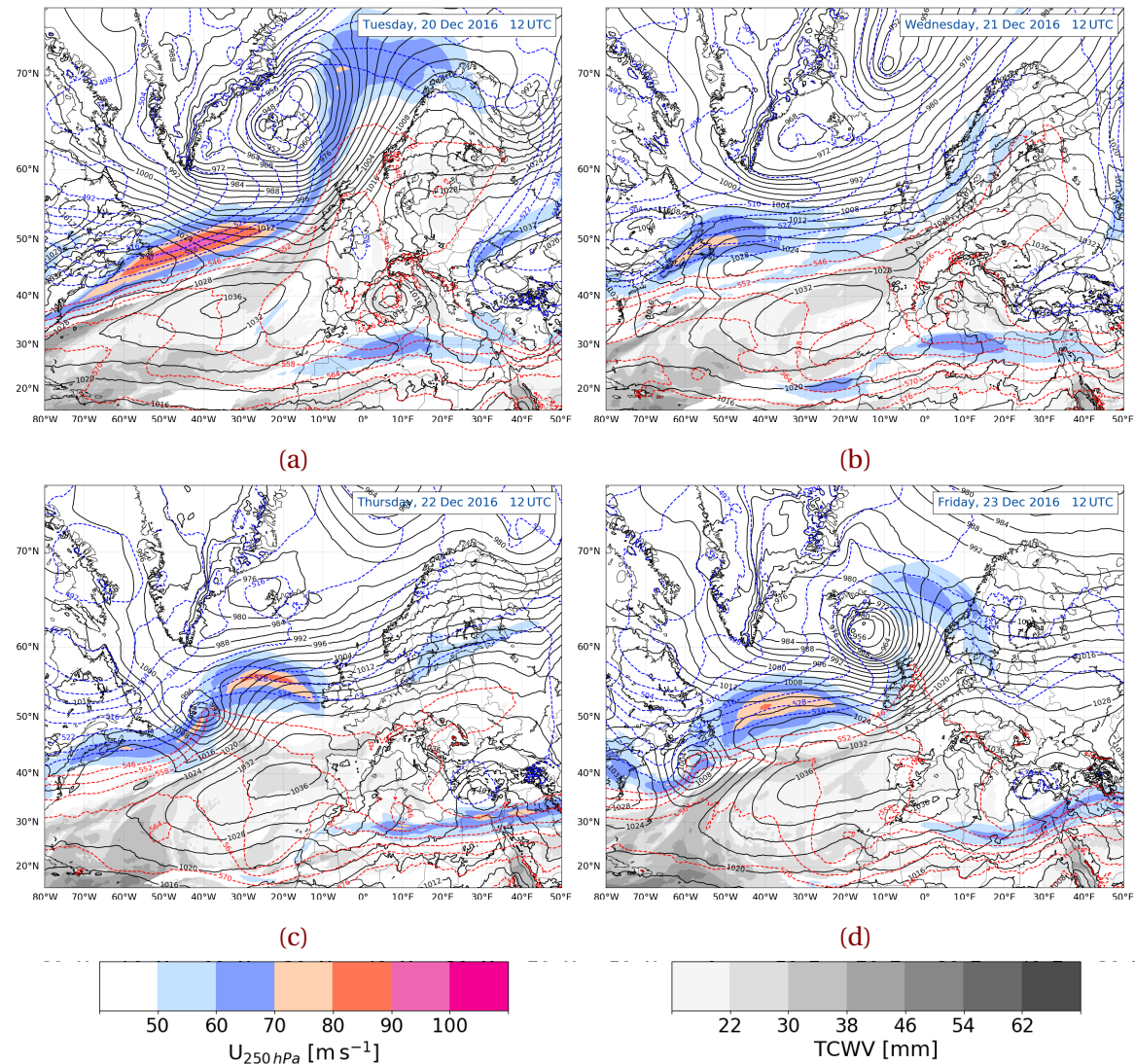


Figure 4.2.1: Dynamic tropopause analysis map, data from ECMWF at 2 PVU. During 20 December 2016 to 27 December 2016. Potential temperature [K] at the 2 PVU surface, shaded according to the colour bar. Total wind, barbs $[\text{m s}^{-1}]$, and 925–850 hPa layer-averaged surface relative vorticity (black contours, every $0.5 \times 10^{-4} \text{ s}^{-1}$).

4.3 THICKNESS, SEA LEVEL PRESSURE, MOISTURE, AND WIND AT 250 hPa

A good overview gives the sea level pressure, 1000 – 500 hPa thickness map and winds at 250 hPa. Figure 4.3.1 shows, that it combines several important features of the vertical distribution within the atmosphere, for example.

Black contour lines indicate sea level pressure in hPa and makes it possible to observe cyclones and anticyclones at the sea surface.



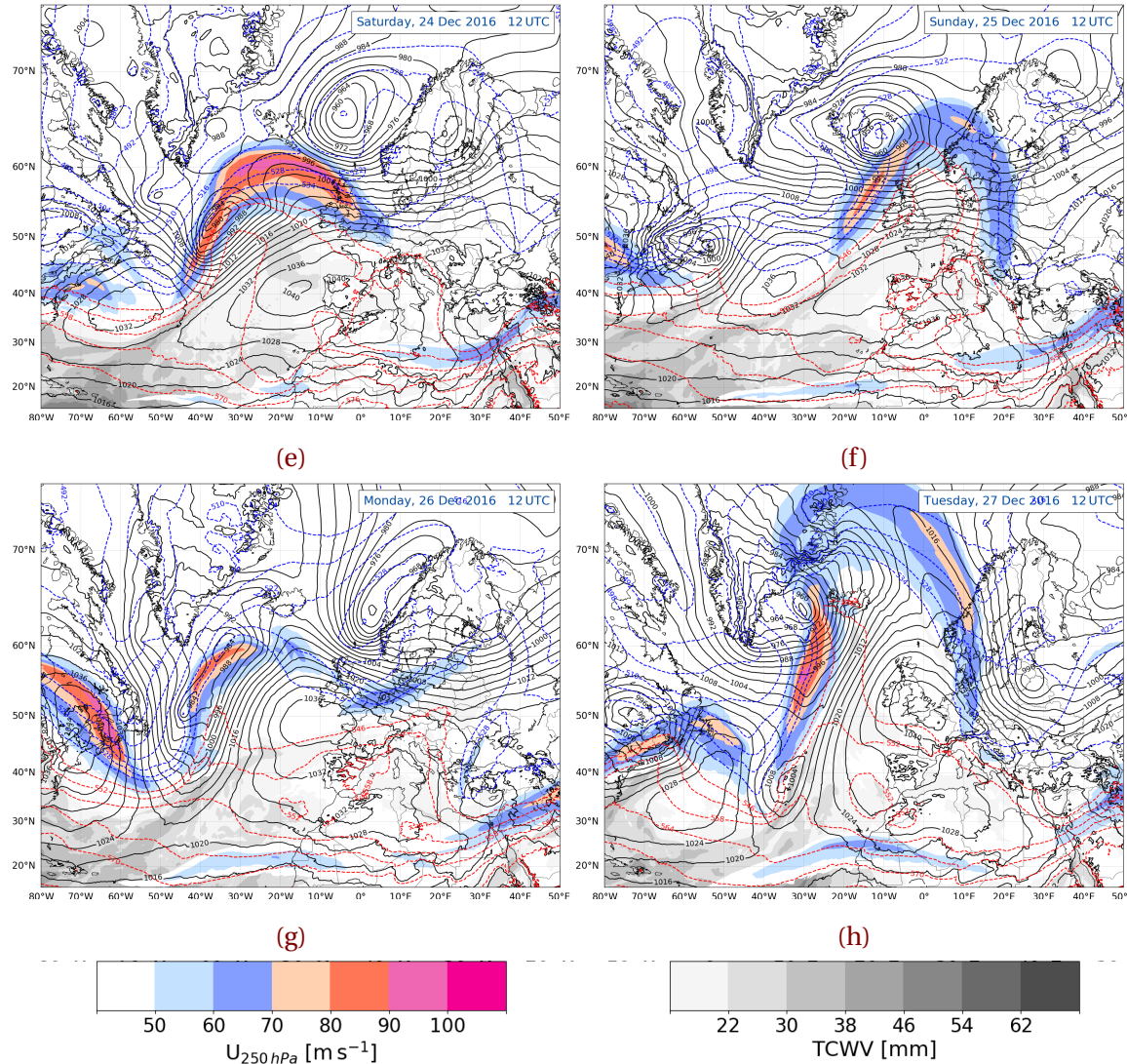


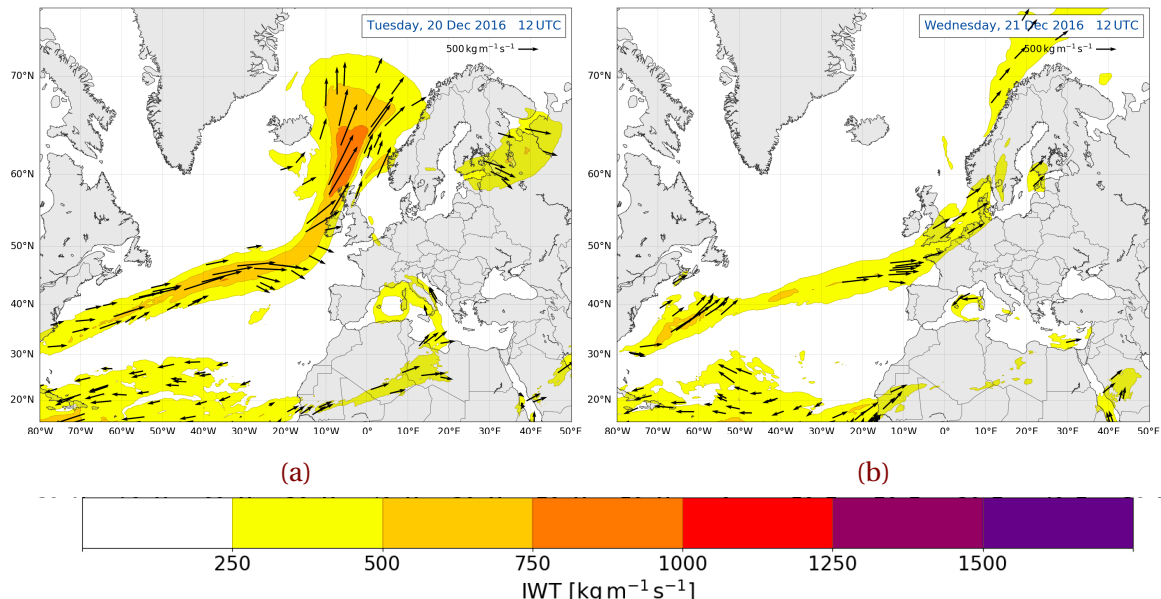
Figure 4.3.1: Jet, thickness, mean sea level pressure, and moisture synoptic analysis, data from ECMWF. During 20 December 2016 to 27 December 2016. 250 hPa wind speed, shaded according to the colour bar, $[\text{m s}^{-1}]$. 1000–500 hPa thickness, dashed contours every 6 dam, MSLP, black contours every 4 hPa, total column water vapour [mm], shaded according the grey scale.

The dashed, coloured contours show the vertical thickness between the 1000 hPa and 500 hPa surface, every 6 dam. The thickness between two pressure levels can be related to the hypsometric equation (Equation (3.4.3)). This is a relation of the mean temperature of the air between two pressure levels. Thus, high values of thickness mean relative warm, moist air (red, dashed). This can then be associated to rain or snow in mid-latitudes, depending on cold or warm air advection.

Gray shaded areas describe total precipitable water in the atmosphere in mm. It is an indicator for the amount of moisture to supply rainfall, and will be used to identify where moisture was present.

Colour shaded contours in Figure 4.3.1 indicate the mid-latitude jet streaks at 250 hPa. Warmer colour is associated with higher wind speeds at this level.

4.4 ATMOSPHERIC RIVER MAP



An atmospheric river (AR) is a filament structure of intense moisture transport from the tropics to higher latitudes. Heavy precipitation can be associated with it, because the air is warm and moist. This can often be observed at mountain ranges at west coasts such as in Norway [include reference here](#). Due to orographic lifting will the moisture be released and follow high amounts of precipitation.

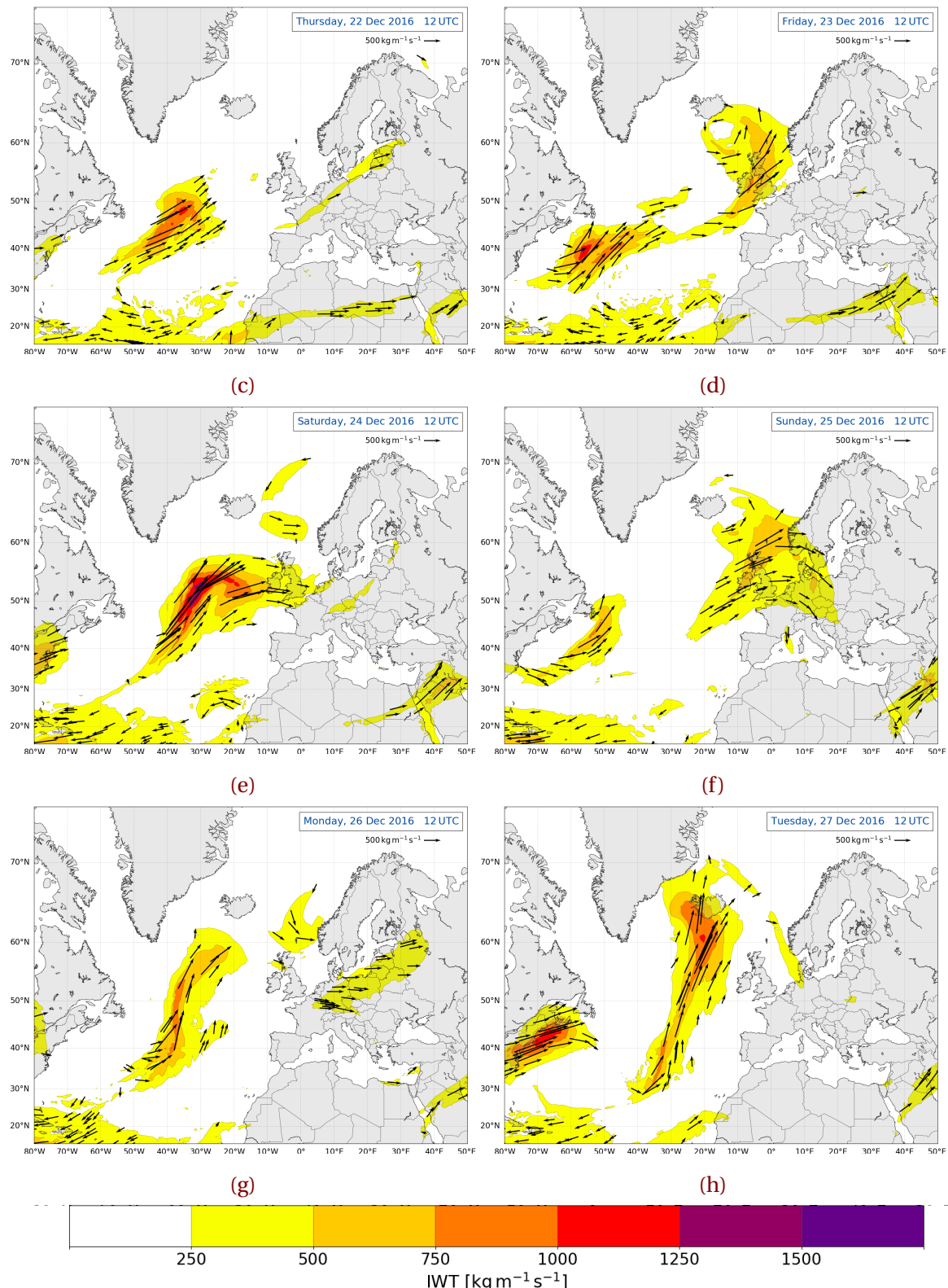


Figure 4.4.1: Atmospheric river analysis map, data from ECMWF. During 20 December 2016 to 27 December 2016. IVT, shaded according to the colour bar [$\text{kg m}^{-1} \text{s}^{-1}$]. Vectors, indicating the direction and magnitude of the IVT.

An atmospheric river is characterised if the integrated vapour transport shows values higher than $250 \text{ kg m}^{-1} \text{ s}^{-1}$ and is a continuous region larger than 2000 km [Rutz et al., 2014]. The integrated vapour transport (IVT) was calculated from the ECMWF data as followed:

$$IVT = \frac{1}{g} \int_{p_{sfc}}^{100 \text{ hPa}} q \mathbf{V} dp \quad [\text{kg m}^{-1} \text{ s}^{-1}] \quad (4.4.1)$$

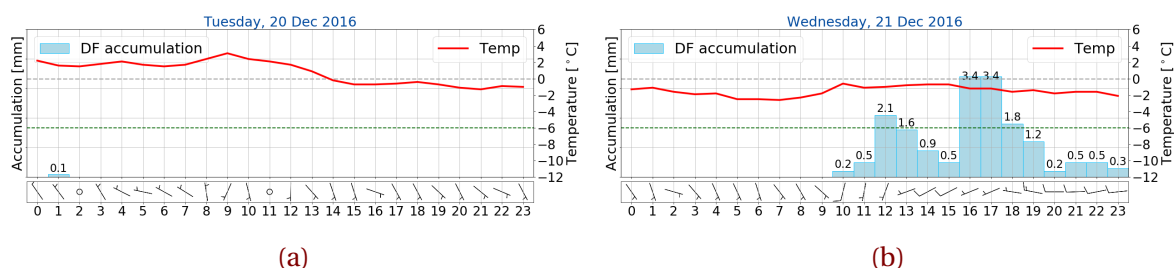
where g is the standard gravity, q the specific humidity, and \mathbf{V} the total wind vector at each pressure level p . The numerical, trapezoidal integration is performed by using data from the surface pressure p_{sfc} to 850 hPa in 50 hPa intervals and from 700 hPa to 100 hPa in 100 hPa intervals.

Figure 4.4.1 shows coloured contours of the integrated vapour transport (IVT) in $\text{kg m}^{-1} \text{ s}^{-1}$, where warmer colours indicate higher IVT. Stream vectors indicate the direction and intensity of the IVT flow.

4.5 OBSERVATIONS AT THE WEATHER MAST

The large scale synoptic analysis will be related to the local weather observations at Haukeliseter.

60 min accumulation is presented as bars in Figure 4.5.1 and will show the continuous precipitation at Haukeliseter during the extreme event. The possible change of precipitation will be investigated with the temperature. Snow fall is likely for temperatures up to 2 °C. The intensity of the storm can be classified by the hourly averaged wind speed and direction as wind barbs in m s^{-1} . To understand which damage a storm can have, Færæas et al. [2016] released a table to associate wind strength with damage (see Table 4.5.1).



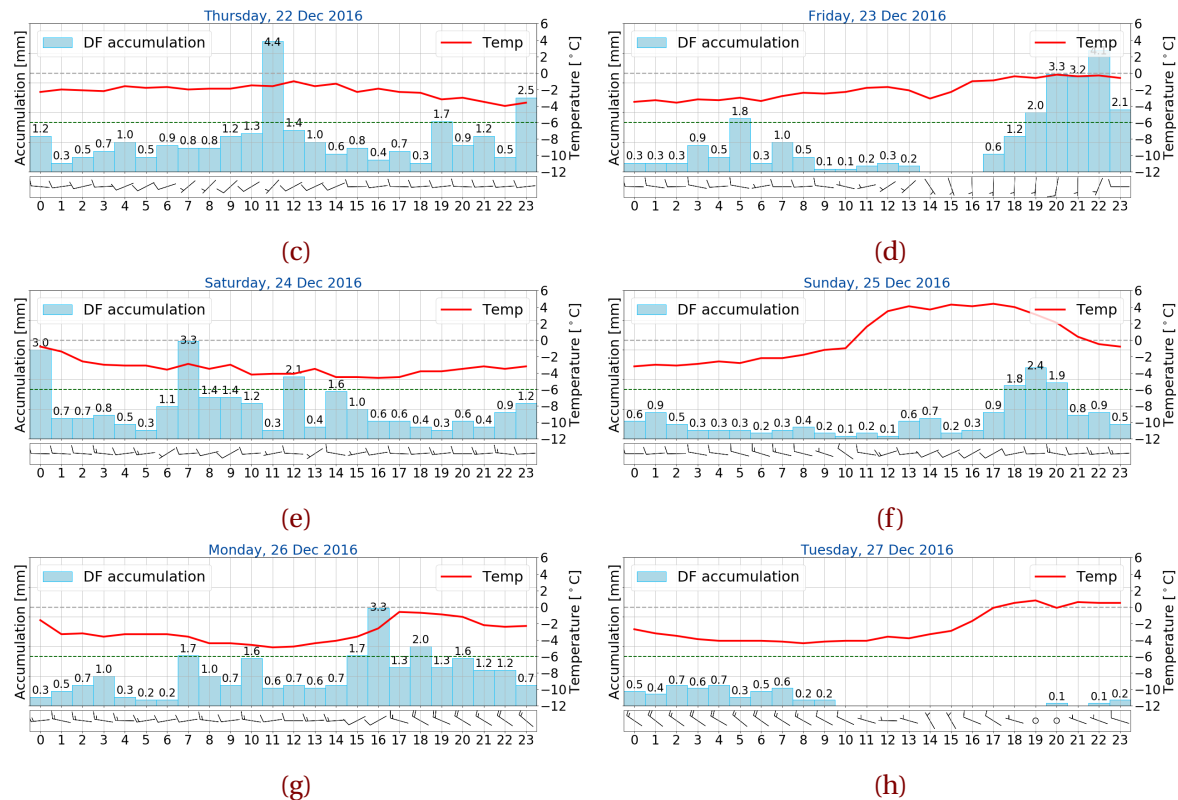


Figure 4.5.1: Observation from the weather mast at Haukeliseterd during 20 December 2016 to 27 December 2016. 60 min total accumulation [mm] in light blue as bar, temperature (red, $^{\circ}\text{C}$), and wind as barbs [m s^{-1}]. Gray dashed line indicates the freezing temperature and the green dashed line the 30-year climate mean temperature at -6°C . Hourly processed data taken from [eklima \[2016\]](#).

Table 4.5.1: Damage related to wind speed, from Færaas et al. [2016].

slight storm	$20.8 \text{ ms}^{-1} - 24.4 \text{ ms}^{-1}$	Large trees sway and hiver. Roofs can blow down.
full storm	$24.5 \text{ ms}^{-1} - 28.4 \text{ ms}^{-1}$	Trees are pulled up with clutter. Big damages to houses.
strong storm	$28.5 \text{ ms}^{-1} - 32.6 \text{ ms}^{-1}$	Extensive damage.
hurricane	$>32.6 \text{ ms}^{-1}$	Unusually large destruction.

4.6 RADIOSONDE FROM STAVANGER

The Appendix B includes images of vertical temperature profiles of Radiosondes from Stavanger, represented in a Skew-T log-P diagram. The vertical profiles extend from surface up to 300 hPa. (Note, that the representation of the vertical scale (in m) differs with each sounding from day to day.)

The vertical temperature distribution will identify the stability of the atmosphere and give information on convection and thickness of clouds. Furthermore, warm air and cold air advection can be identified by observing the change of wind with height.

Black and green line represent the atmospheric and dew-point temperature, respectively.

4.7 LARGE SCALE CIRCULATION

Everything has to get into relation with the Radiosondes, Figure B.0.1. How to do that? Any suggestions? They took me some time to make, so I want to include them!

21 December 2016

The dynamic tropopause map in Figure 4.2.1b shows that Norway is influenced by a change of elevated tropopause to a suppressed tropopause during 20 December 2016 to 21 December 2016. Hence the potential vorticity changed from positive to negative at the tropopause and cold air stretches right over Norway. A good amount of moisture is

transported from the low latitudes to high latitudes, influencing Norway's west coast. This can be seen in the surface maps (Figure 4.3.1b) as well as in the atmospheric river maps (Figure 4.4.1b). The westerly flow in Figure 4.3.1b is conducive to orographic lifting. The precipitation was probably snow when having a look at the moisture content and the cold air. The change from warm air to cold air can also be observed in the time series of temperature in Figure 4.5.1b. And the westerly flow, combined with a good amount of vapour transport from the tropics led to orographic lifting and precipitation at the Haukeliseter site. At around 60°W a formation of a cyclone at the baroclinic zone can be implied.

22 December 2016

Twenty-four hours later the analysis shows from 22 December 2016 phasing between the surface relative vorticity and the baroclinic zone at 50°N in the DT. The centre of the surface low is directly located below the temperature gradient at the 2 PVU surface, hence this is good for synoptic lifting. Furthermore, the strongest baroclinicity is observed on the south west side of the surface low. The synoptic map of the geopotential thickness and the surface pressure show the beginning of the frontal boundaries in Figure 4.3.1c. At the same time shows the AR map, Figure 4.4.1c, large values just at the baroclinic zone, where the low pressure is beginning to form. **Help?! Does that lead to even more lifting in this area? Or does it just mean that the cyclone gets a good amount of moisture?!**. Norway is located in a cold area. The continues precipitation observed at Haukeliseter (Figure 4.5.1c) is associated with the westerly flow which is conducive to orographic lifting, and therefore moisture release.

23 December 2016

The begin of the ridging on the 22 December 2016 is more pronounced 24 h later. The warmer air pushes away the cold air, which covered Norway. The low pressure system moved north-east, and lies south of Iceland. The occluded front of this system passes through Haukeliseter, which is why a temperature 'jump' observed at 14 UTC. After this, Southern Norway is influenced by the warm sector, monitored as a temperature increase. The AR, as well as the total column water vapour amount in Figure 4.4.1d and Figure 4.3.1d,

respectively show the amount of moisture, transported from low latitudes.

At the same time forms a second cyclone at the baroclinic zone at 40° N. The atmospheric river map (Figure 4.4.1d) indicates a large amount of moisture at this latitude. Again, moist, warm air is conducive to intensify the surface cyclone. In addition, shows the DT map a phasing between the low level vorticity and the upper level baroclinic zone.

24 December 2016

After the passage of the cold front over Norway, Scandinavia is within colder air (compare Figure 4.2.1e and Figure 4.3.1e for 24 December 2016). Over the Atlantic warmer air starts to push the colder air northward. **something something with the low level vorticity and lifting; lifting at the right entrance region of the jet streak, and very high IVT.**

At Haukeliseter negative temperature up to -4°C is observed, compare Figure 4.5.1e. The westerly flow is again conducive for orographic lifting and associated precipitation.

25 December 2016

Twenty-four hours later the ridge is more pronounced and covers large parts of Norway. The surface low south-east of Iceland has build its frontal boundaries, which can be seen in the low-level vorticity of Figure 4.2.1f. The warm front lies west of Haukeliseter and starts to be observed at the measurement site (compare Figure 4.5.1f for 25 December 2016). Figure 4.4.1f indicating the integrated vapour transport shows that a lot of moisture is transported from the Atlantic, towards Great Britain and south-western Norway. Together with the lifting at the surface boundary a sufficient amount of precipitation is observed. Since the ridging brings more moist (Figure 4.4.1f), warm air (Figure 4.2.1f) and Norway lies in a warm sector (Figure 4.3.1f) the assumption will be made, that the precipitation changed from solid to liquid.

26 December 2016

Within the next twenty-four hours the cold front passed through (temperature change in Figure 4.5.1g for 25 December 2016 to 26 December 2016). Norway is covered in cold air (Figure 4.2.1g). The surface low-level indicates the occlusion of the cyclone and therefore a weakening. The wind is still from the west which is helpful for orographic lifting. The

moisture content is still present but much weaker and smaller in extend. Since Norway is covered in cold air, the temperature is below zero and the precipitation had to be solid.

27 December 2016

The images of 27 December 2016 show that the storm passed and disappeared. Southern Norway lies in cold air (Figure 4.2.1h), but on the right exit region of the jet (\rightarrow sinking motion of cold air), compare 4.3.1h. A small amount of moisture is present (Figure 4.4.1h). Because of the wind change from west to north-west follows that orographic lifting is not present and the precipitation amount decreases at the end of the storm.

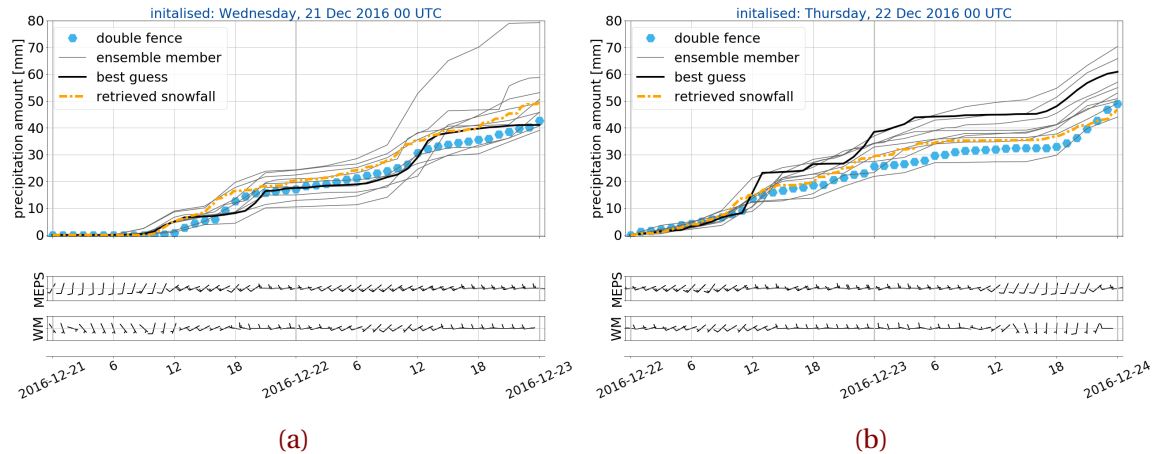
CHAPTER 5: RESULTS

The overleaf file from the Results is here:

<https://www.overleaf.com/15070250fhqztnygzmn>

- 21 December 2016 has convective storm from 9 UTC to 13 UTC then pulsing
- on 23 December 2016 convective storm from 16 UTC to 0 UTC
- connection with wind Figures 5.2.1a to 5.2.1f
- **pick interesting days:**
 - 21 December 2016, because change from convective storm to pulsing event → put in the connection with wind. MEPS does catch convective part, but not as strong. High SWC_{MEPS} at 20 UTC
 - 22 December 2016, because SWC_{RETRIEVAL} almost same as SWC_{MEPS}, only 2 h shift
 - 24 December 2016, because SWC_{MEPS} almost as pulsing as SWC_{RETRIEVAL} just not as strong. Also overestimation of surface snowfall from MEPS Figure 5.1.1d. All 10 ensemble members have pulsing. Most interesting EM5, EM7 (not shown). Figure 5.2.1d looks interesting, good catch between the two systems.
 - 25 December 2016, because MEPS covers the LWC at the same time as retrieval, but the retrieval does not see the snow above → weakness of retrieval is shown even though weak. See: Figure 5.3.1e and C.0.1e. Also it has the overestimation at the surface Figure 5.1.1e
 - 26 December 2016 Figure 5.2.1f see overestimation of SWP_{MEPS} in scatter and in wind. Is it somehow connected?!

5.1 SURFACE SNOWFALL ACCUMULATION



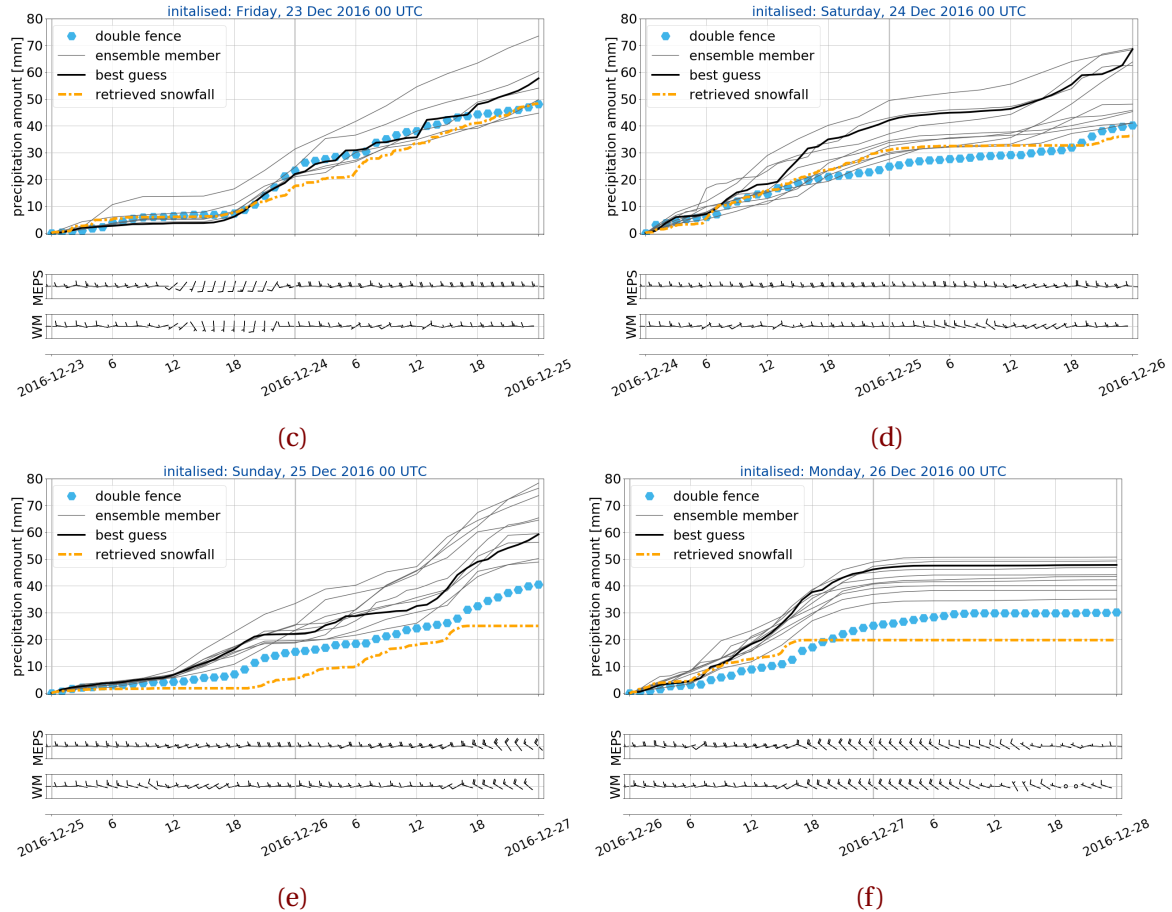


Figure 5.1.1: Surface snowfall accumulation. Representing the values from the double fence in light blue, hexagons; optimal estimation retrieval output at snow layer height 800 m in dashed orange; and ensemble member deterministic forecast, initialised at 0 UTC in black and its nine perturbed ensemble members in grey. Underneath are the associated wind bars from the deterministic MEPS forecast and the weather mast at 10 m height.

5.2 SWP AND RELATION TO WIND

5.3 SWC AND SWP FROM MEPS AND THE OPTIMAL ESTIMATION RETRIEVAL

Images for the liquid water content evaluated in MEPS can be found in Appendix C.

Table 5.3.1: Maximum values of the snow water and liquid water content from the retrieval and MEPS

	SWC [kg m ⁻³]	HEIGHT [m]	TIME	LWC [kg m ⁻³]	HEIGHT [m]	TIME
Wed, 21 Dec 2016						
RETRIEVAL	1.08	600.0	16 UTC			
MEPS	2.11	1400.0	20 UTC	0.15	2200. 0	23 UTC
Thu, 22 Dec 2016						
RETRIEVAL	1.46	1200.0	10 UTC			
MEPS	1.35	1400.0	12 UTC	0.20	2000.0	02 UTC
Fri, 23 Dec 2016						
RETRIEVAL	0.91	600.0	23 UTC			
MEPS	0.54	400.0	20 UTC	0.14	1000.0	15 UTC
Sat, 24 Dec 2016						
RETRIEVAL	1.39	1000.0	06 UTC			
MEPS	0.73	1400.0	17 UTC	0.33	1200.0	09 UTC
Sun, 25 Dec 2016						
RETRIEVAL	0.69	1400.0	21 UTC			
MEPS	0.50	800.0	20 UTC	0.34	200.0	17 UTC
Mon, 26 Dec 2016						
RETRIEVAL	1.25	600.0	15 UTC			
MEPS	1.55	1000.0	11 UTC	0.17	2400.0	09 UTC

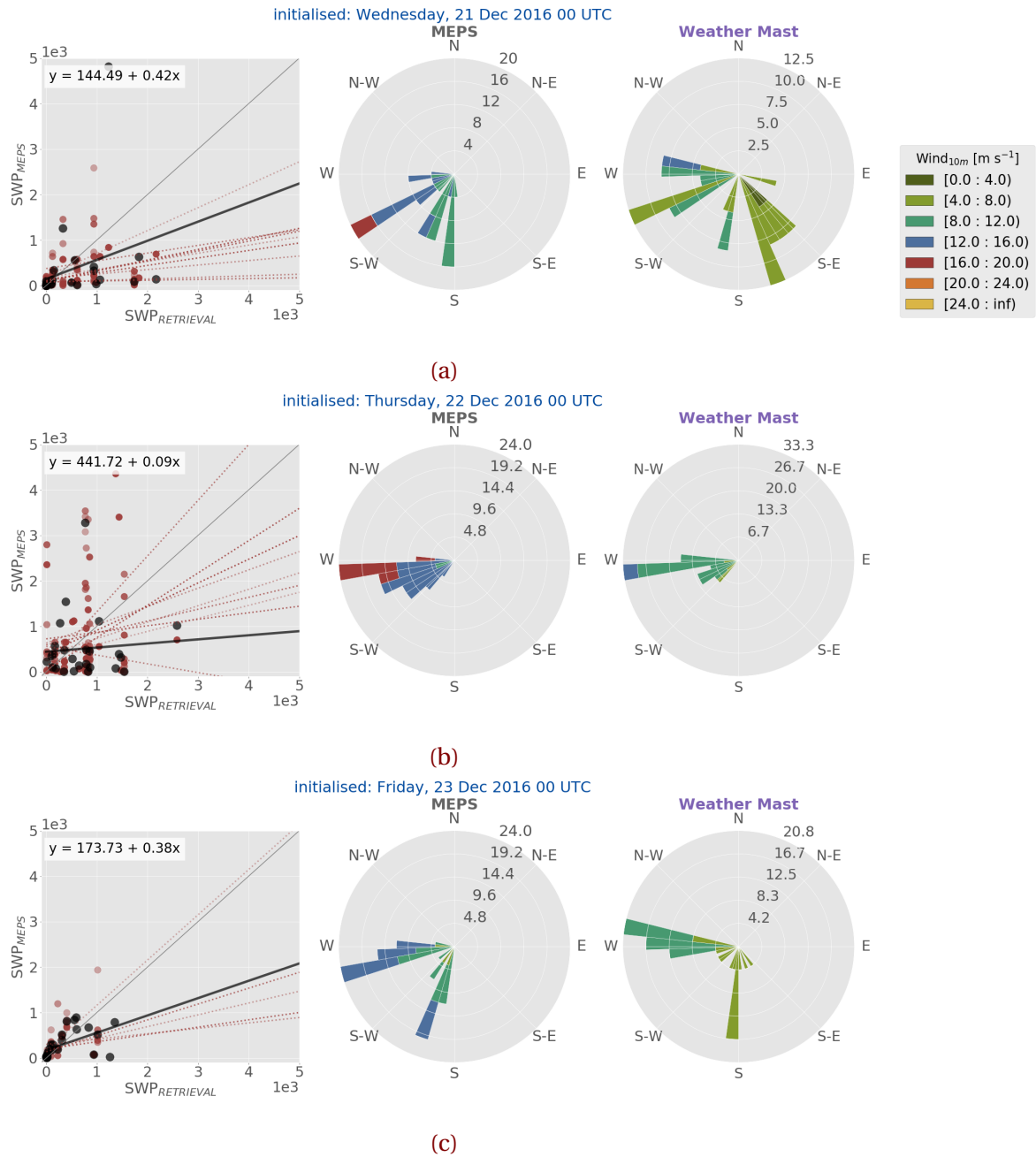
5.4 WEDNESDAY, 21 December 2016

Convection appears: see Figure 5.4.1a and 5.4.1b, also Figure B.0.1b

5.5 THURSDAY, 22 December 2016

5.6 SATURDAY, 24 December 2016

5.7 SATURDAY, 25 December 2016



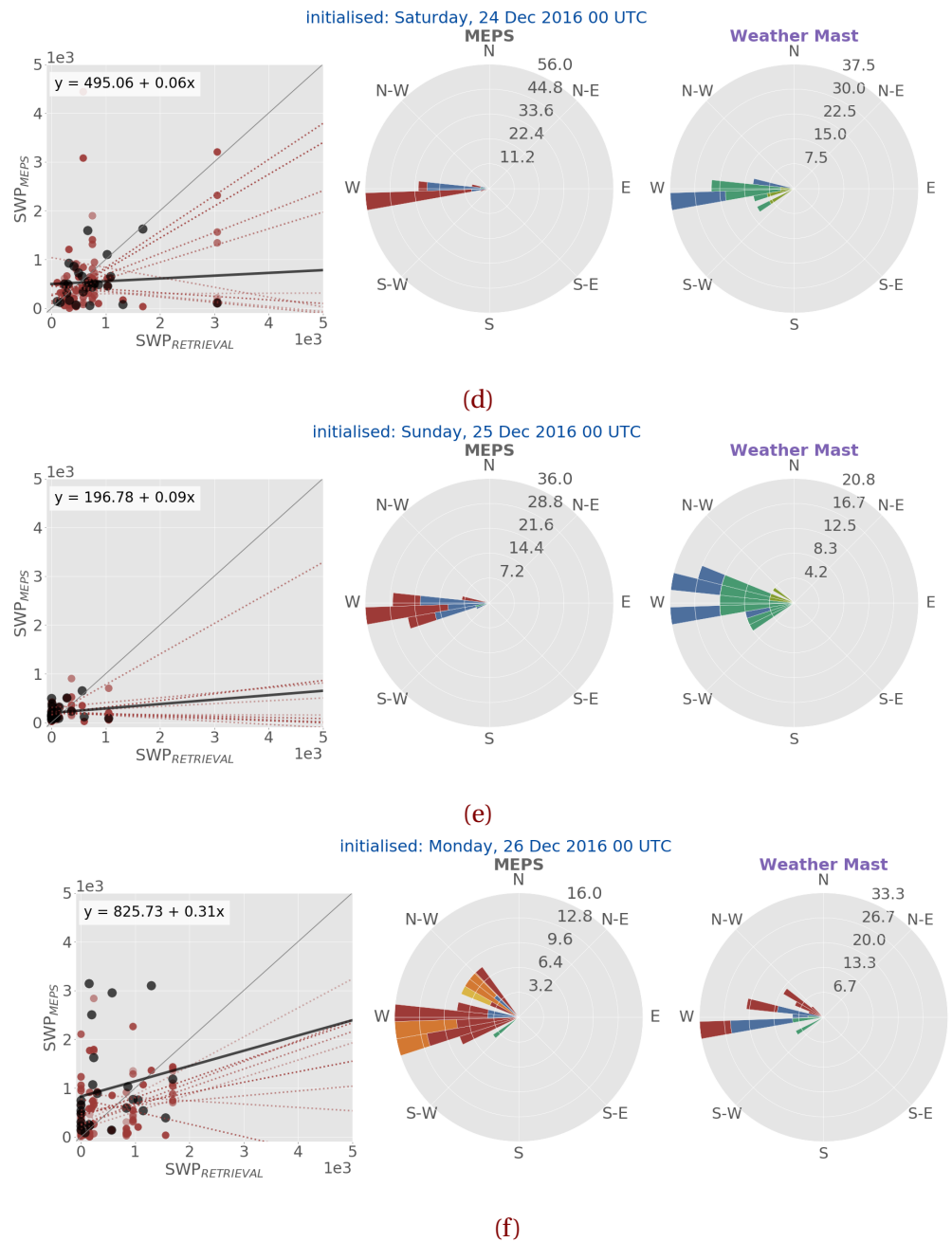
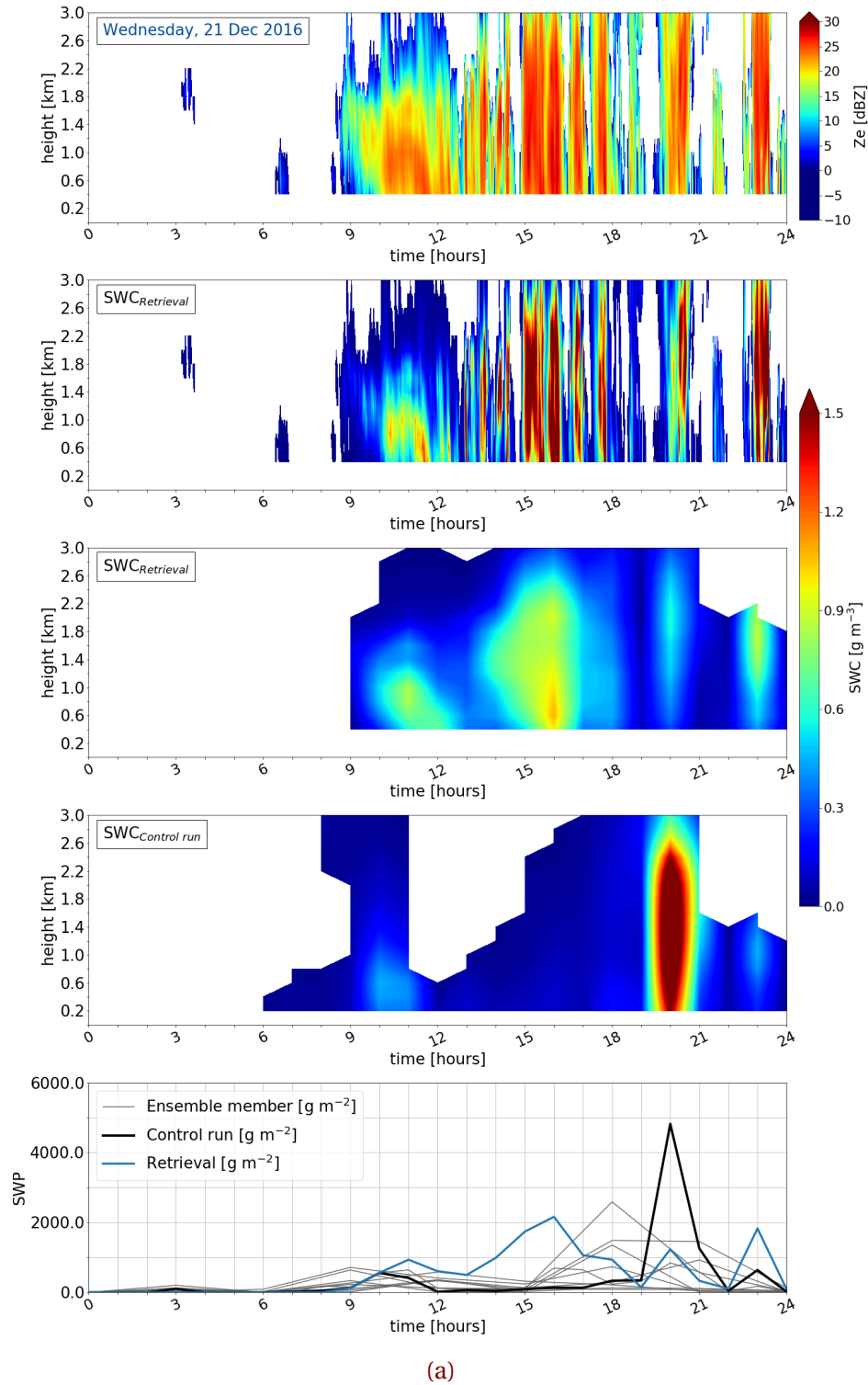
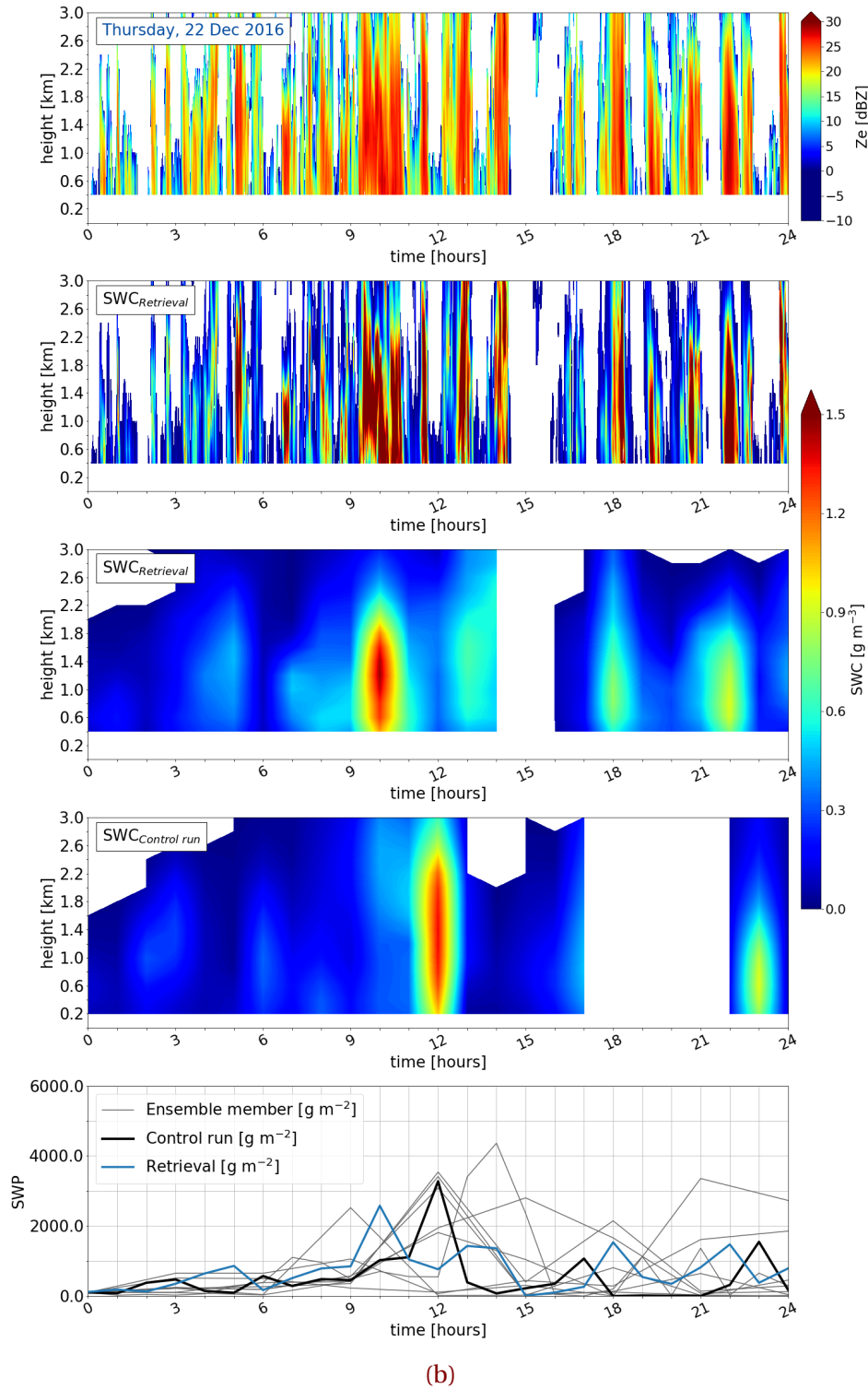
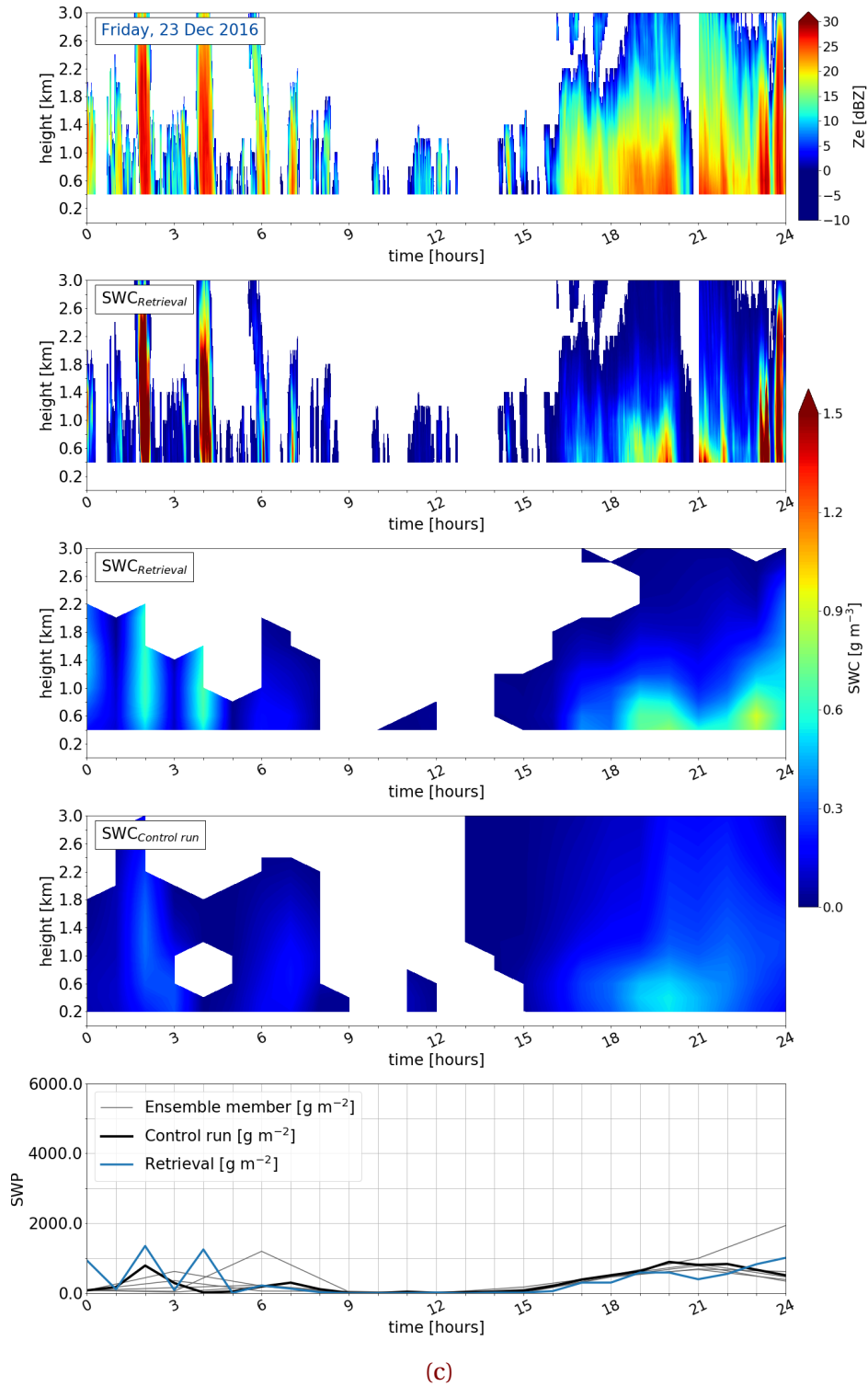
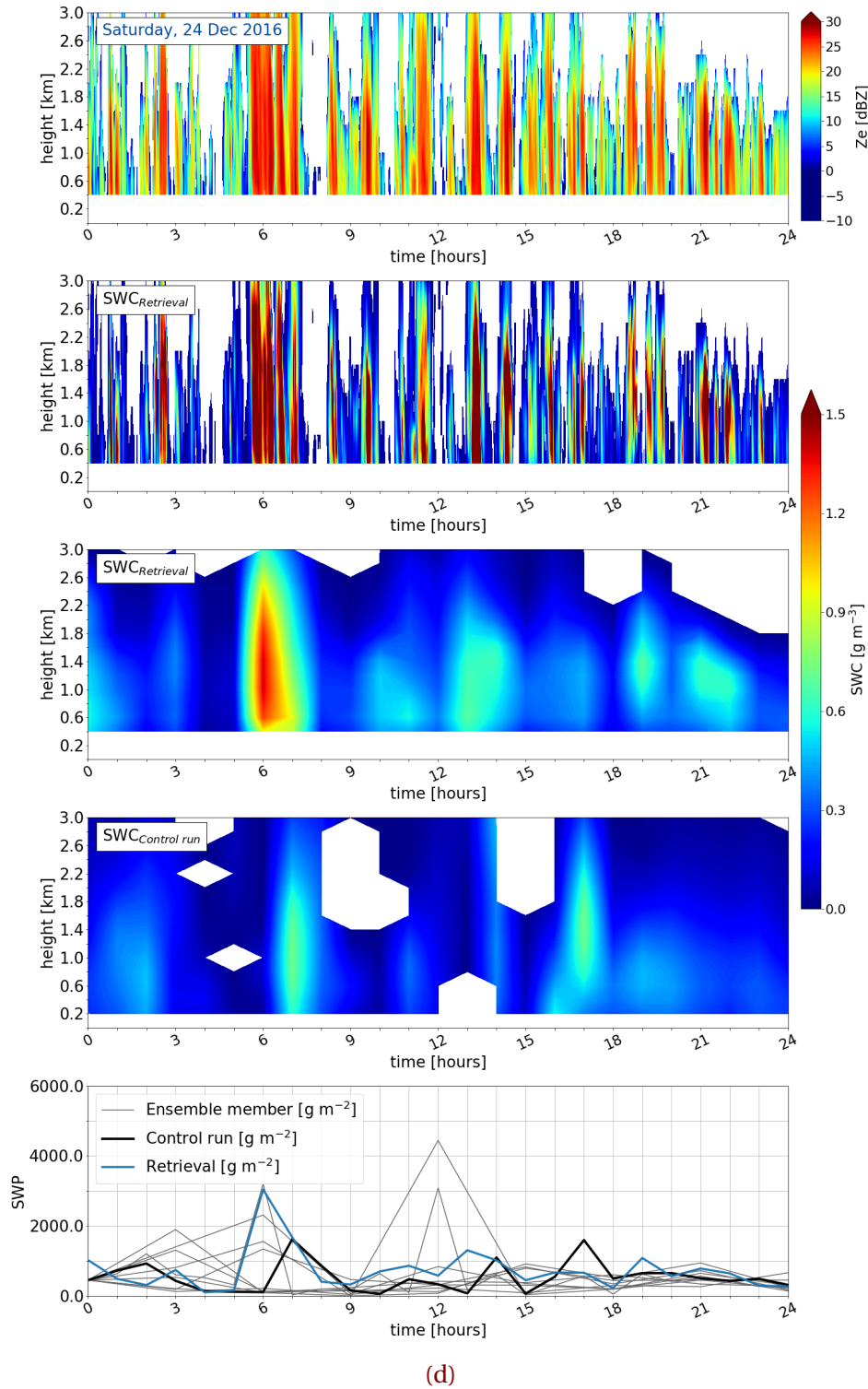


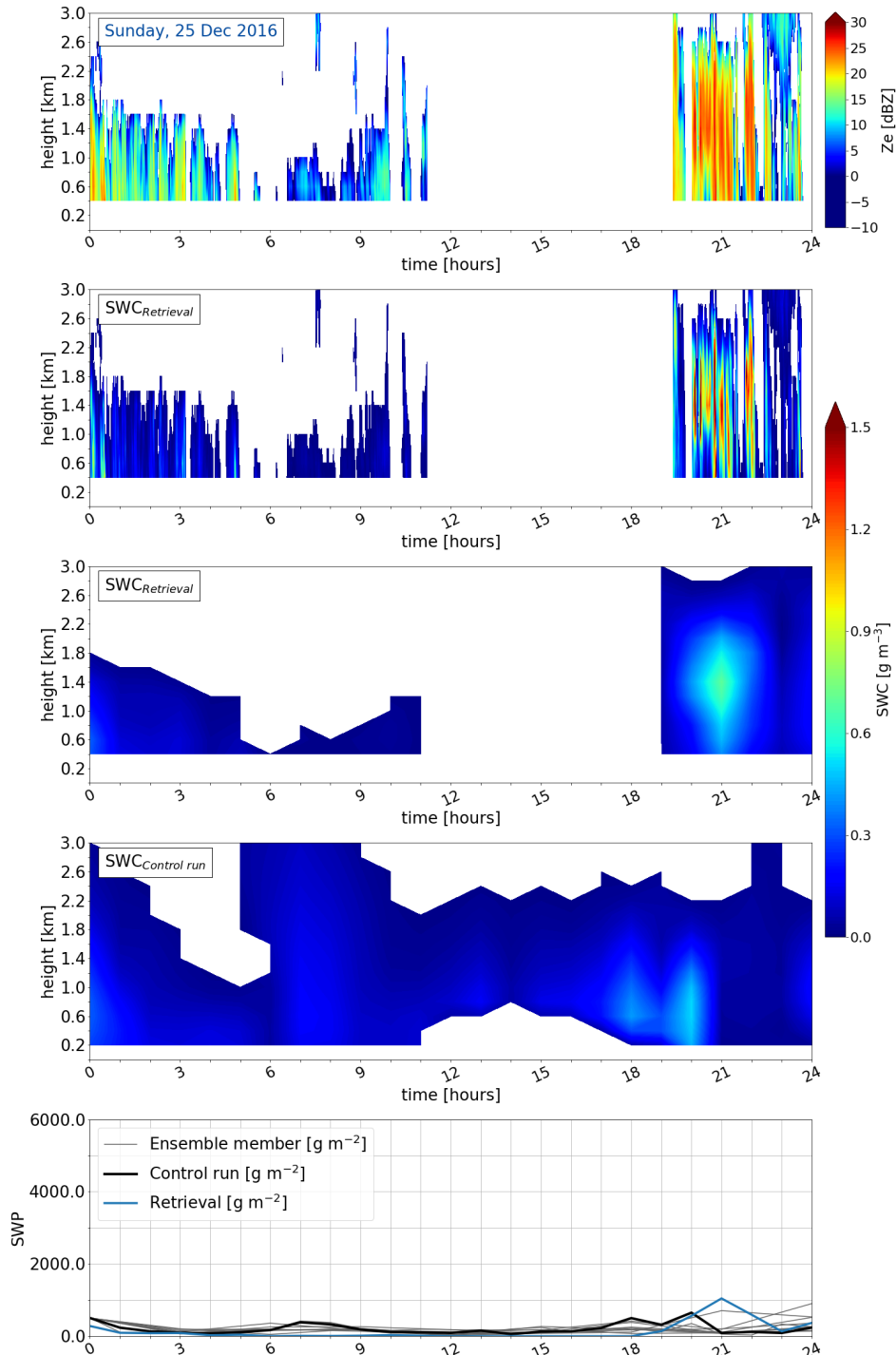
Figure 5.2.1: Left panel: Scatter plot of SWP from retrieval and the 10 ensemble members initialised at 0 UTC as dots. Black dots and respective best fit (black line) indicate the relation between the deterministic forecast and the retrieval. Red dashed line representing the best fit between the SWP values from MEPS (ensemble member 2 to 10) and the retrieval. 2nd panel: hourly deterministic forecast wind roses from MEPS initialised at 0 UTC. 3rd panel: 10 m observed wind at the Haukeliseter measurement site, wind speeds according to the colorbar.



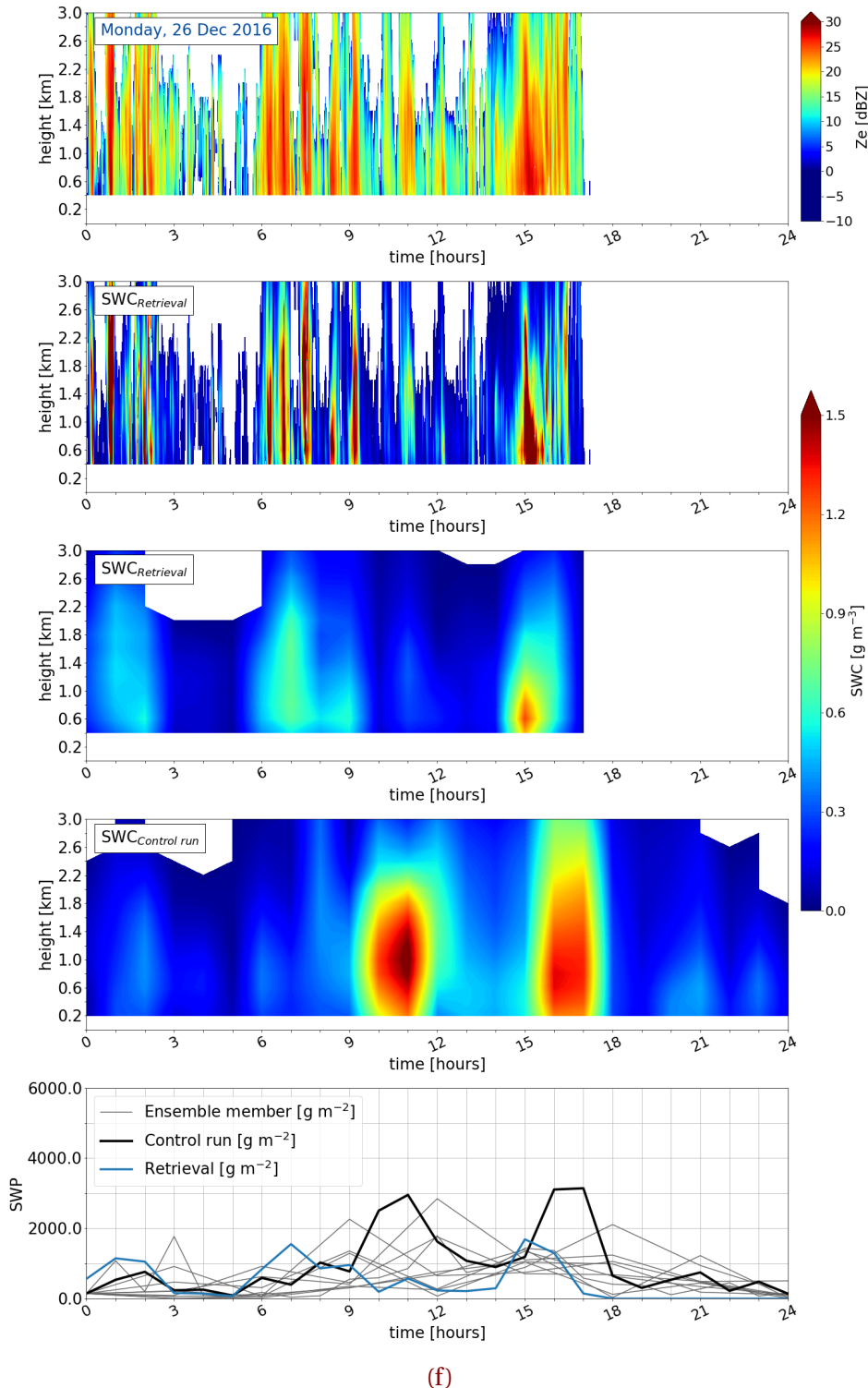








(e)



(f)

Figure 5.3.1: Upper panel: MRR reflectivity in dBZ. 2nd panel: SWC optimal estimation retrieval output every second in gm^{-3} . 3rd panel: hourly-averaged SWC optimal estimation retrieval output. 4th panel: 200 m-averaged SWC deterministic forecast from MEPS. Lowest panel: SWP from MEPS, initialised at 0 UTC. Black line represents the deterministic forecast and the grey lines the nine perturbed members. In blue the SWP from the averaged retrieval output.

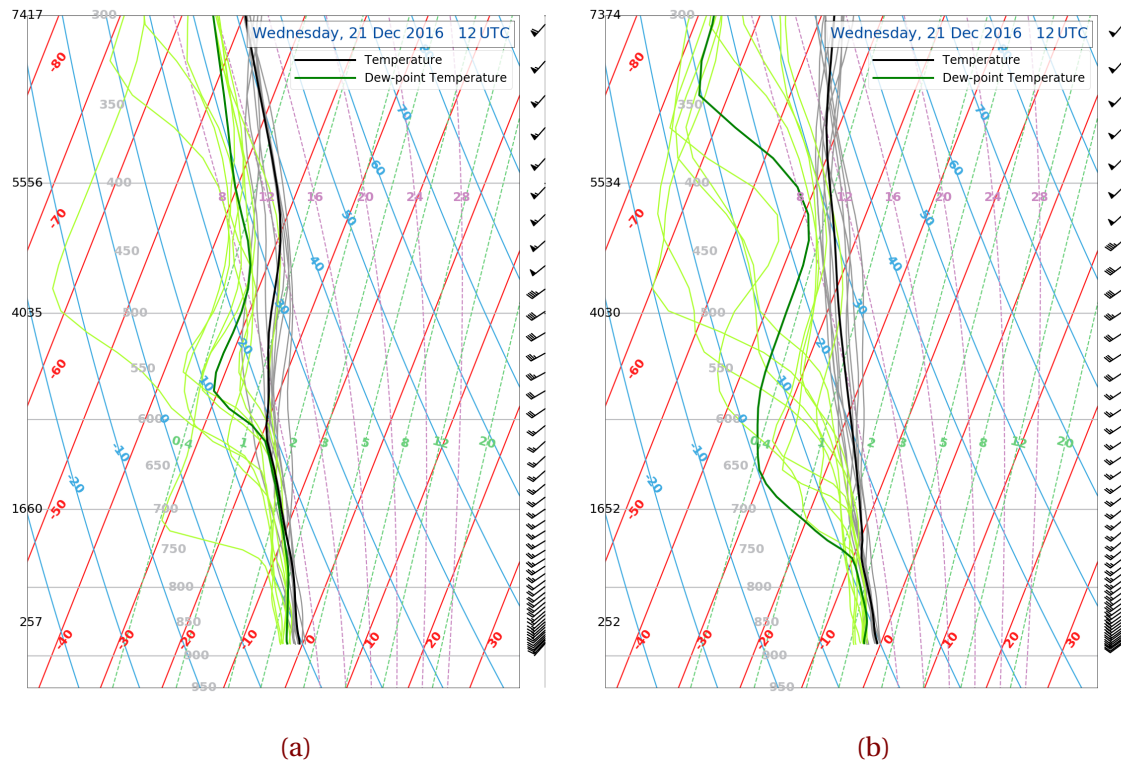


Figure 5.4.1: Vertical temperature profiles produced with MEPS. **a** is initialised: Tuesday, 20 December 2016 0 UTC. **b** is initialised: Wednesday, 21 December 2016 0 UTC.

REFERENCES

- G. Caniaux, J-L. Redelsperger, and J-P. Lafore. A Numerical Study of the Stratiform Region of a Fast-Moving Squall Line. Part I: General Description and Water and Heat Budgets. *J. Atmos. Sci.*, 51(14):2046–2074, July 1994. ISSN 0022-4928. doi: [10.1175/1520-0469\(1994\)051<2046:ANSOTS>2.0.CO;2](https://doi.org/10.1175/1520-0469(1994)051<2046:ANSOTS>2.0.CO;2). URL [https://journals.ametsoc.org/doi/abs/10.1175/1520-0469\(1994\)051%3C2046:ANSOTS%3E2.0.CO;2](https://journals.ametsoc.org/doi/abs/10.1175/1520-0469(1994)051%3C2046:ANSOTS%3E2.0.CO;2).
- S. J. Cooper, N. B. Wood, and T. S. L'Ecuyer. A variational technique to estimate snowfall rate from coincident radar, snowflake, and fall-speed observations. *Atmos. Meas. Tech.*, 10(7):2557–2571, July 2017. ISSN 1867-8548. doi: [10.5194/amt-10-2557-2017](https://doi.org/10.5194/amt-10-2557-2017). URL <https://www.atmos-meas-tech.net/10/2557/2017/>.
- R. J. Doviak and D. S. Zrnic. *Doppler Radar and Weather Observations*. Courier Corporation, 1993. ISBN 978-0-486-45060-5. Google-Books-ID: [ispLkPX9n2UC](#).
- eklima. Norwegian Meteorological Institute, 2016. URL http://sharki.oslo.dnmi.no/portal/page?_pageid=73,39035,73_39049&_dad=portal&_schema=PORTAL.
- E. Farestveit. 80.000 mista radioen under ekstremvêret, December 2016. URL <https://www.nrk.no/hordaland/80.000-mista-radioen-under-ekstremveret-1.13294980>.
- A. Færaas, A. Rommetveit, J. Duesund, and E. Senel. «Urd» har nådd orkan styrke – flytter seg mot Østlandet, December 2016. URL http://www.yr.no/artikkkel/_urd_-har-nadd-orkan-styrke--flytter-seg-mot-ostlandet-1.13292245.
- T. J. Garrett, C. Fallgatter, K. Shkurko, and D. Howlett. Fall speed measurement and high-resolution multi-angle photography of hydrometeors in free fall. *Atmos. Meas. Tech.*, 5

- (11):2625–2633, November 2012. ISSN 1867-8548. doi: [10.5194/amt-5-2625-2012](https://doi.org/10.5194/amt-5-2625-2012). URL <https://www.atmos-meas-tech.net/5/2625/2012/>.
- Geonor Inc. T-200b All Weather Precipitation – Rain Gauge, 2015. URL <http://geonor.com/live/products/weather-instruments/t-200b-weather-precipitation-rain-gauge/>.
- K. L. S. Gunn and T. W. R. East. The microwave properties of precipitation particles. *Q. J. Royal Meteorol. Soc.*, 80(346):522–545, 1954.
- M. Homleid and F. T. Tveter. Verification of operational weather prediction models september to november 2015. *METInfo Rep*, 16:2016, 2016. URL https://www.met.no/publikasjoner/met-info/met-info-2016/_attachment/download/b0463915-cba0-42ac-8539-4233ae2bf01c:3d71565a27f88085373199a33ab8569151c144e9/MET-info-22-2016.pdf.
- B. J. Hoskins, M. E. McIntyre, and A. W. Robertson. On the use and significance of isentropic potential vorticity maps. *Q. J. Royal Meteorol. Soc.*, 111(470):877–946, October 1985. ISSN 1477-870X. doi: [10.1002/qj.49711147002](https://doi.org/10.1002/qj.49711147002). URL <http://onlinelibrary.wiley.com/doi/10.1002/qj.49711147002/abstract>.
- D. Hudak, H. Barker, P. Rodriguez, and D. Donovan. The Canadian CloudSat Validation Project. *4th ERAD*, September 2006. URL <http://www.crahi.upc.edu/ERAD2006/proceedingsMask/00165.pdf>. Barcelona, Spain.
- H. Joos and H. Wernli. Influence of microphysical processes on the potential vorticity development in a warm conveyor belt: a case-study with the limited-area model COSMO. *Q. J. Royal Meteorol. Soc.*, 138(663):407–418, January 2012. ISSN 00359009. doi: [10.1002/qj.934](https://doi.org/10.1002/qj.934). URL <http://doi.wiley.com/10.1002/qj.934>.
- Kartverket. Norgeskart, November 2018. URL http://www.norgeskart.no/?_ga=2.7509489.291164698.1524482471-1352211079.1517515119#!?project=seeiendom&layers=1002,1015&zoom=4&lat=7197864.00&lon=396722.00.
- M. S. Kulie and R. Bennartz. Utilizing Spaceborne Radars to Retrieve Dry Snowfall. *J. Appl. Meteor. Climatol.*, 48(12):2564–2580, January 2009. ISSN 1558-8424. doi:

- 10.1175/2009JAMC2193.1. URL <http://journals.ametsoc.org/doi/abs/10.1175/2009JAMC2193.1>.
- M. A. Ø. Køltzow. MetCoOp EPS - A convection permitting ensemble prediction system, October 2017.
- D. Lamb and J. Verlinde. *Physics and Chemistry of Clouds*. Cambridge University Press, April 2011. ISBN 978-1-139-50094-4. Google-Books-ID: H97QKhe16aUC.
- T. S. L'Ecuyer. AOS 441 - Satellite and Radar Meteorology. January 2017. URL <https://lecuyer.aos.wisc.edu/aos441>.
- T. S. L'Ecuyer and G. L. Stephens. An Estimation-Based Precipitation Retrieval Algorithm for Attenuating Radars. *J. Appl. Meteor.*, 41(3):272–285, January 2002. ISSN 0894-8763. doi: [10.1175/1520-0450\(2002\)041<0272:AEBPRA>2.0.CO;2](https://doi.org/10.1175/1520-0450(2002)041<0272:AEBPRA>2.0.CO;2). URL [http://journals.ametsoc.org/doi/abs/10.1175/1520-0450\(2002\)041%3C0272:AEBPRA%3E2.0.CO%3B2](http://journals.ametsoc.org/doi/abs/10.1175/1520-0450(2002)041%3C0272:AEBPRA%3E2.0.CO%3B2).
- Liu G. Deriving snow cloud characteristics from CloudSat observations. *J. Geophys. Res. Atmos.*, 113(D8), September 2008. ISSN 0148-0227. doi: [10.1029/2007JD009766](https://doi.org/10.1029/2007JD009766). URL <https://agupubs.onlinelibrary.wiley.com/doi/abs/10.1029/2007JD009766>.
- U. Lohmann, F. Lüönd, and F. Mahrt. *An Introduction to Clouds: From the Microscale to Climate*. Cambridge University Press, June 2016. ISBN 978-1-107-01822-8. Google-Books-ID: KR1CDAAAQBAJ.
- P. Markowski and Y. Richardson. *Mesoscale Meteorology in Midlatitudes*. John Wiley & Sons, September 2011. ISBN 978-1-119-96667-8. Google-Books-ID: MDeYosfLLEYC.
- J. E. Martin. *Mid-Latitude Atmospheric Dynamics: A First Course*. Wiley, May 2006. ISBN 978-0-470-86466-1.
- M. McCumber, W.-K. Tao, J. Simpson, R. Penc, and S.-T. Soong. Comparison of Ice-Phase Microphysical Parameterization Schemes Using Numerical Simulations of Tropical Convection. *J. Appl. Meteor.*, 30(7):985–1004, July 1991. ISSN 0894-8763. doi: [10.1175/1520-0450-30.7.985](https://doi.org/10.1175/1520-0450-30.7.985). URL [https://journals.ametsoc.org/doi/abs/10.1175/1520-0450-30.7.985](https://doi.org/10.1175/1520-0450-30.7.985).

- MetCoOp Wiki. Description of MEPS, December 2017. URL <https://metcoop.smhi.se/dokuwiki/nwp/metcoop/>.
- Meteorologische Messtechnik GmbH METEK. Micro Rain Radar MRR-2, October 2010. URL <http://metek.de/wp-content/uploads/2014/05/Metek-Micro-Rain-Radar-MRR-2-Datasheet.pdf>.
- Meteo France. The Meso-NH Atmospheric Simulation System: Scientific Documentation, Part III: Physics, January 2009.
- Meteorologene. "Her kommer #Urd! Selve Lavtrykksenteret treffer Møre og Romsdal, men den sterkeste vinden kommer sør for Stad. #SørNorge" 26 December 2016, 9:34am, 2016. URL <https://twitter.com/Meteorologene>.
- M. Müller, M. Homleid, K.-I. Ivarsson, M. A. \O. Køltzow, M. Lindskog, K. H. Midtbø, U. Andrae, T. Aspelien, L. Berggren, D. Bjørge, P. Dahlgren, J. Kristiansen, R. Randriamampianina, M. Ridal, and O. Vignes. AROME-MetCoOp: A Nordic Convective-Scale Operational Weather Prediction Model. *Wea. Forecasting*, 32(2):609–627, January 2017. ISSN 0882-8156. doi: [10.1175/WAF-D-16-0099.1](https://doi.org/10.1175/WAF-D-16-0099.1). URL <http://journals.ametsoc.org/doi/abs/10.1175/WAF-D-16-0099.1>.
- A. J. Newman, P. A. Kucera, and L. F. Bliven. Presenting the Snowflake Video Imager (SVI). *J. Atmos. Oceanic Technol.*, 26(2):167–179, February 2009. ISSN 0739-0572. doi: [10.1175/2008JTECHA1148.1](https://doi.org/10.1175/2008JTECHA1148.1). URL <https://journals.ametsoc.org/doi/abs/10.1175/2008JTECHA1148.1>.
- L. Norin, A. Devasthale, T. S. L'Ecuyer, N. B. Wood, and M. Smalley. Intercomparison of snowfall estimates derived from the CloudSat Cloud Profiling Radar and the ground-based weather radar network over Sweden. *Atmos. Meas. Tech.*, 8(12):5009–5021, December 2015. ISSN 1867-8548. doi: [10.5194/amt-8-5009-2015](https://doi.org/10.5194/amt-8-5009-2015). URL <https://www.atmos-meas-tech.net/8/5009/2015/>.
- Norwegian Meteorological Institute. MET Norway Thredds Service, 2016. URL <http://thredds.met.no/thredds/catalog/meps25epsarchive/catalog.html>.
- A.-M. Olsen and M. Granerød. Ekstremværrapport. Hendelse: Urd 26. desember met. info. no. 18/2017 ISSN X METEOROLOGI Bergen, - PDF, September

2017. URL <http://docplayer.me/48734203-Ekstremvaerrapport-hendelse-urd-26-desember-met-info-no-18-2017-issn-x-meteorologi-bergen.html>.
- C. Palerme, Ch. Genthon, C. Claud, J. E. Kay, N. B. Wood, and T. L'Ecuyer. Evaluation of current and projected Antarctic precipitation in CMIP5 models. *Clim. Dyn.*, 48(1-2): 225–239, January 2017. ISSN 0930-7575, 1432-0894. doi: [10.1007/s00382-016-3071-1](https://doi.org/10.1007/s00382-016-3071-1). URL <https://link.springer.com/article/10.1007/s00382-016-3071-1>.
- K. Pedersen and A. Rommetveit. Hva er et «ekstremvær»?, November 2013. URL http://www.yr.no/artikkelen/hva-er-et-_ekstremvaer__-1.7890946.
- M. C. Peel, B. L. Finlayson, and T. A. Mcmahon. Updated world map of the Köppen-Geiger climate classification. *Hydrology and Earth System Sciences Discussions*, 4(2):439–473, March 2007. URL <https://hal.archives-ouvertes.fr/hal-00298818>.
- J.-P. Pinty and P. Jabouille. A mixed-phased cloud parameterization for use in a mesoscale non-hydrostatic model: Simulations of a squall line and of orographic precipitation. pages 217–220. Amer. Meteor. Soc., 1998.
- R. E. Rinehart. *Radar for Meteorologists: Or You, Too, Can be a Radar Meteorologist*. Rinehart Publications, 2010. ISBN 978-0-9658002-3-5. Google-Books-ID: VqatcQAACAAJ.
- C. D. Rodgers. *Inverse Methods for Atmospheric Sounding: Theory and Practice*. World Scientific, 2000. ISBN 978-981-02-2740-1. Google-Books-ID: FjxqDQAAQBAJ.
- J. J. Rutz, W. J. Steenburgh, and F. M. Ralph. Climatological Characteristics of Atmospheric Rivers and Their Inland Penetration over the Western United States. *Mon. Wea. Rev.*, 142(2):905–921, January 2014. ISSN 0027-0644. doi: [10.1175/MWR-D-13-00168.1](https://doi.org/10.1175/MWR-D-13-00168.1). URL <https://journals.ametsoc.org/doi/abs/10.1175/MWR-D-13-00168.1>.
- S. Ruud, H. Carr Ekroll, A. Bakke Foss, H. O. Torgersen, and P. Annar Holm. To tonn tungt skilt blåste ned da ekstremværet traff Oslo og Østlandet i natt, December 2016. URL <https://www.aftenposten.no/article/ap-2z6wy.html>.
- G. L. Stephens. *Remote Sensing of the Lower Atmosphere: An Introduction*. Oxford University Press, 1994. ISBN 978-0-19-508188-6. Google-Books-ID: 2FcRAQAAIAAJ.

- G. L. Stephens and N. B. Wood. Properties of Tropical Convection Observed by Millimeter-Wave Radar Systems. *Monthly Weather Review*, 135(3):821–842, March 2007. ISSN 0027-0644, 1520-0493. doi: [10.1175/MWR3321.1](https://doi.org/10.1175/MWR3321.1). URL <http://journals.ametsoc.org/doi/abs/10.1175/MWR3321.1>.
- G. L. Stephens, D. G. Vane, R. J. Boain, G. G. Mace, K. Sassen, Z. Wang, A. J. Illingworth, E. J. O’Connor, W. B. Rossow, S. L. Durden, S. D. Miller, R. T. Austin, A. Benedetti, C. Mitrescu, and the CloudSat Science Team. THE CLOUDSAT MISSION AND THE A-TRAIN: A New Dimension of Space-Based Observations of Clouds and Precipitation. *Bull. Am. Meteorol. Soc.*, 83(12):1771–1790, December 2002. ISSN 0003-0007, 1520-0477. doi: [10.1175/BAMS-83-12-1771](https://doi.org/10.1175/BAMS-83-12-1771). URL <http://journals.ametsoc.org/doi/10.1175/BAMS-83-12-1771>.
- M. A. Wolff. WMO Solid Precipitation Intercomparison Experiment (WMO-SPICE), Ch. 4.2.4 Precipitation measurements in areas with high winds and/or complex terrain. unpublished, 2018.
- M. A. Wolff, R. Brækkan, K. Isaksen, and E. Ruud. A new testsite for wind correction of precipitation measurements at a mountain plateau in southern Norway. In *Proceedings of WMO Technical Conference on Meteorological and Environmental Instruments and Methods of Observation (TECO-2010). Instruments and Observing Methods Report*, 2010.
- M. A. Wolff, K. Isaksen, R. Brækkan, E. Alfnæs, A. Petersen-Øverleir, and E Ruud. Measurements of wind-induced loss of solid precipitation: description of a Norwegian field study. *Hydrol. Res.*, 44(1):35–43, February 2013. ISSN 0029-1277, 2224-7955. doi: [10.2166/nh.2012.166](https://doi.org/10.2166/nh.2012.166). URL <http://hr.iwaponline.com/content/44/1/35>.
- M. A. Wolff, K. Isaksen, A. Petersen-Øverleir, K. Ødemark, T. Reitan, and R. Brækkan. Derivation of a new continuous adjustment function for correcting wind-induced loss of solid precipitation: results of a Norwegian field study. *Hydrol. Earth Syst. Sci.*, 19(2):951–967, February 2015. ISSN 1607-7938. doi: [10.5194/hess-19-951-2015](https://doi.org/10.5194/hess-19-951-2015). URL <https://www.hydrol-earth-syst-sci.net/19/951/2015/>.
- N. B. Wood. *Estimation of snow microphysical properties with application to millimeter-wavelength radar retrievals for snowfall rate*. Ph.D., Colorado State University,

2011. URL https://dspace.library.colostate.edu/bitstream/handle/10217/48170/Wood_colostate_0053A_10476.pdf?sequence=1&isAllowed=y.
- N. B. Wood, T. S. L'Ecuyer, F. L. Bliven, and G. L. Stephens. Characterization of video disdrometer uncertainties and impacts on estimates of snowfall rate and radar reflectivity. *Atmos. Meas. Tech.*, 6(12):3635–3648, December 2013a. ISSN 1867-8548. doi: [10.5194/amt-6-3635-2013](https://doi.org/10.5194/amt-6-3635-2013). URL <http://www.atmos-meas-tech.net/6/3635/2013/>.
- N. B. Wood, T. S. L'Ecuyer, D. G. Vane, G. L. Stephens, and P. Partain. Level 2c snow profile process description and interface control document. Technical Report, 2013b. URL http://www.cloudsat.cira.colostate.edu/sites/default/files/products/files/2C-SNOW-PROFILE_PDICD.P_R04.20130210.pdf.
- N. B. Wood, T. S. L'Ecuyer, A. J. Heymsfield, G. L. Stephens, D. R. Hudak, and P. Rodriguez. Estimating snow microphysical properties using collocated multisensor observations. *J. Geophys. Res. Atmos.*, 119(14):8941–8961, July 2014. ISSN 2169-8996. doi: [10.1002/2013JD021303](https://doi.org/10.1002/2013JD021303). URL <http://onlinelibrary.wiley.com/doi/10.1002/2013JD021303/abstract>.
- N. B. Wood, T. S. L'Ecuyer, A. J. Heymsfield, and G. L. Stephens. Microphysical Constraints on Millimeter-Wavelength Scattering Properties of Snow Particles. *J. Appl. Meteor. Climatol.*, 54(4):909–931, January 2015. ISSN 1558-8424. doi: [10.1175/JAMC-D-14-0137.1](https://doi.org/10.1175/JAMC-D-14-0137.1). URL <http://journals.ametsoc.org/doi/10.1175/JAMC-D-14-0137.1>.

APPENDIX A: SCATTERING MODEL

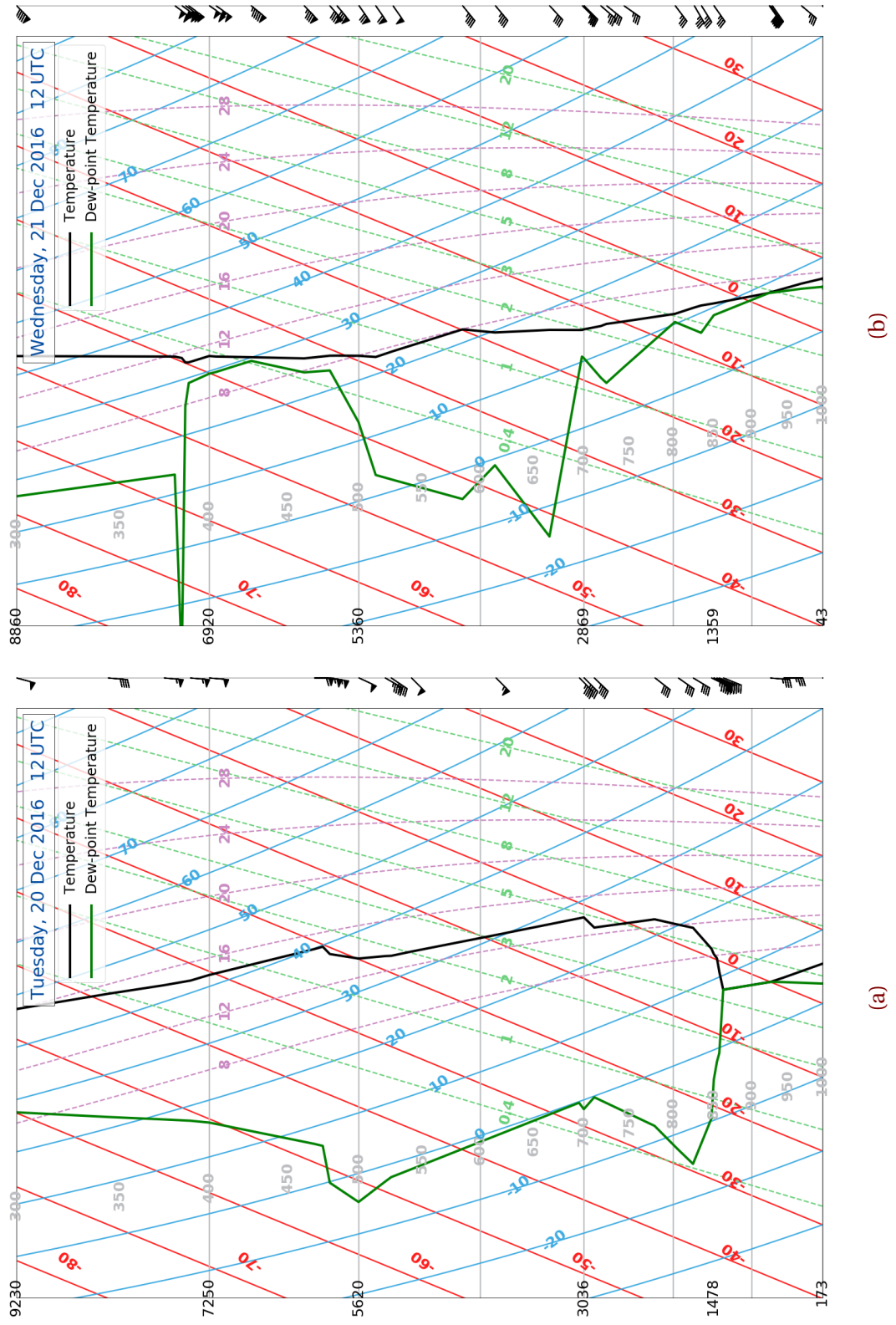
Table A.0.1: Branched 6-arm spatial particle with porosities, 2D, mass oriented scattering scheme at 24.0GHz. \mathbf{r} , particle size of the snow particle; $\mathbf{m}(\mathbf{r})$, particle mass; $\sigma_{bk}(\mathbf{r})$ and $\sigma_{ext}(\mathbf{r})$, backscattering and extinction cross-section, respectively.

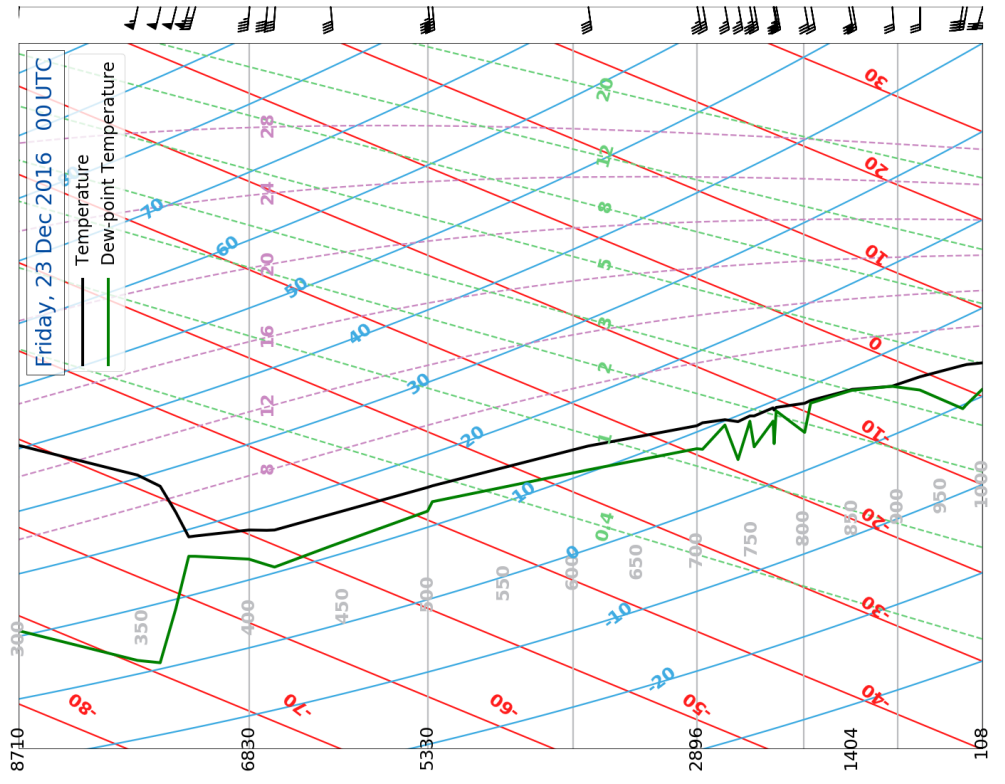
r [μm]	$\mathbf{m}(\mathbf{r})$ [kg]	$\sigma_{bk}(\mathbf{r})$ [m ⁻²]	$\sigma_{ext}(\mathbf{r})$ [m ⁻²]	\mathbf{r} [μm]	$\mathbf{m}(\mathbf{r})$ [kg]	$\sigma_{bk}(\mathbf{r})$ [m ⁻²]	$\sigma_{ext}(\mathbf{r})$ [m ⁻²]
35.27	1.68529 × 10 ⁻¹⁰	8.85311 × 10 ⁻¹⁷	4.85381 × 10 ⁻¹⁷	428.20	3.01577 × 10 ⁻⁷	1.7526 × 10 ⁻¹⁰	5.67393 × 10 ⁻¹⁰
41.73	2.79128 × 10 ⁻¹⁰	2.00612 × 10 ⁻¹⁶	1.28776 × 10 ⁻¹⁶	463.00	3.81242 × 10 ⁻⁷	3.58177 × 10 ⁻¹⁰	8.76374 × 10 ⁻¹⁰
47.87	4.21355 × 10 ⁻¹⁰	4.792 × 10 ⁻¹⁶	2.9959 × 10 ⁻¹⁶	496.90	4.71265 × 10 ⁻⁷	5.86279 × 10 ⁻¹⁰	1.30417 × 10 ⁻⁹
53.76	5.96809 × 10 ⁻¹⁰	1.02733 × 10 ⁻¹⁵	6.08871 × 10 ⁻¹⁶	530.10	5.72178 × 10 ⁻⁷	8.50141 × 10 ⁻¹⁰	1.8862 × 10 ⁻⁹
59.45	8.07074 × 10 ⁻¹⁰	1.68272 × 10 ⁻¹⁵	1.09633 × 10 ⁻¹⁵	562.60	6.84002 × 10 ⁻⁷	1.04566 × 10 ⁻⁹	2.60854 × 10 ⁻⁹
70.34	1.3368 × 10 ⁻⁹	5.7444 × 10 ⁻¹⁵	3.61096 × 10 ⁻¹⁵	594.50	8.07074 × 10 ⁻⁷	1.54514 × 10 ⁻⁹	3.68176 × 10 ⁻⁹
80.69	2.01798 × 10 ⁻⁹	1.0899 × 10 ⁻¹⁴	6.93961 × 10 ⁻¹⁵	625.80	9.41379 × 10 ⁻⁷	1.61704 × 10 ⁻⁹	4.48578 × 10 ⁻⁹
90.63	2.85939 × 10 ⁻⁹	2.244 × 10 ⁻¹⁴	1.42249 × 10 ⁻¹⁴	656.60	1.08733 × 10 ⁻⁶	2.10709 × 10 ⁻⁹	5.71184 × 10 ⁻⁹
100.20	3.86421 × 10 ⁻⁹	3.7814 × 10 ⁻¹⁴	2.73019 × 10 ⁻¹⁴	687.00	1.24546 × 10 ⁻⁶	3.31567 × 10 ⁻⁹	7.85938 × 10 ⁻⁹
109.50	5.04313 × 10 ⁻⁹	7.05869 × 10 ⁻¹⁴	5.36211 × 10 ⁻¹⁴	717.00	1.41584 × 10 ⁻⁶	3.73598 × 10 ⁻⁹	9.50817 × 10 ⁻⁹
118.60	6.40785 × 10 ⁻⁹	1.16874 × 10 ⁻¹³	9.74644 × 10 ⁻¹⁴	746.50	1.59789 × 10 ⁻⁶	4.40591 × 10 ⁻⁹	1.14824 × 10 ⁻⁸
127.40	7.94266 × 10 ⁻⁹	1.67227 × 10 ⁻¹³	1.56602 × 10 ⁻¹³	775.60	1.79214 × 10 ⁻⁶	5.1432 × 10 ⁻⁹	1.37371 × 10 ⁻⁸
144.50	1.15894 × 10 ⁻⁸	3.41952 × 10 ⁻¹³	4.19048 × 10 ⁻¹³	804.40	1.99928 × 10 ⁻⁶	4.21261 × 10 ⁻⁹	1.59603 × 10 ⁻⁸
160.90	1.60002 × 10 ⁻⁸	7.30397 × 10 ⁻¹³	1.05187 × 10 ⁻¹²	832.90	2.2194 × 10 ⁻⁶	7.0875 × 10 ⁻⁹	1.90438 × 10 ⁻⁸
176.80	2.12278 × 10 ⁻⁸	1.13638 × 10 ⁻¹²	2.00359 × 10 ⁻¹²	861.10	2.45255 × 10 ⁻⁶	7.606 × 10 ⁻⁹	2.17023 × 10 ⁻⁸
192.30	2.73147 × 10 ⁻⁸	2.05333 × 10 ⁻¹²	3.63531 × 10 ⁻¹²	888.90	2.69784 × 10 ⁻⁶	9.61605 × 10 ⁻⁹	2.52476 × 10 ⁻⁸
236.50	5.08103 × 10 ⁻⁸	5.94138 × 10 ⁻¹²	1.5256 × 10 ⁻¹¹	916.50	2.95703 × 10 ⁻⁶	1.20108 × 10 ⁻⁸	2.91329 × 10 ⁻⁸
278.10	8.26154 × 10 ⁻⁸	1.57715 × 10 ⁻¹¹	4.31927 × 10 ⁻¹¹	943.80	3.22922 × 10 ⁻⁶	1.29326 × 10 ⁻⁸	3.30911 × 10 ⁻⁸
317.70	1.23171 × 10 ⁻⁷	3.68719 × 10 ⁻¹¹	9.71916 × 10 ⁻¹¹	970.80	3.51437 × 10 ⁻⁶	1.53246 × 10 ⁻⁸	3.82595 × 10 ⁻⁸
355.80	1.73012 × 10 ⁻⁷	6.46005 × 10 ⁻¹¹	1.89057 × 10 ⁻¹⁰	997.60	3.81353 × 10 ⁻⁶	1.32687 × 10 ⁻⁸	4.344 × 10 ⁻⁸
392.60	2.32439 × 10 ⁻⁷	1.29191 × 10 ⁻¹⁰	3.5246 × 10 ⁻¹⁰				

APPENDIX B: SKEW-T LOG-P DIAGRAM FROM STAVANGER

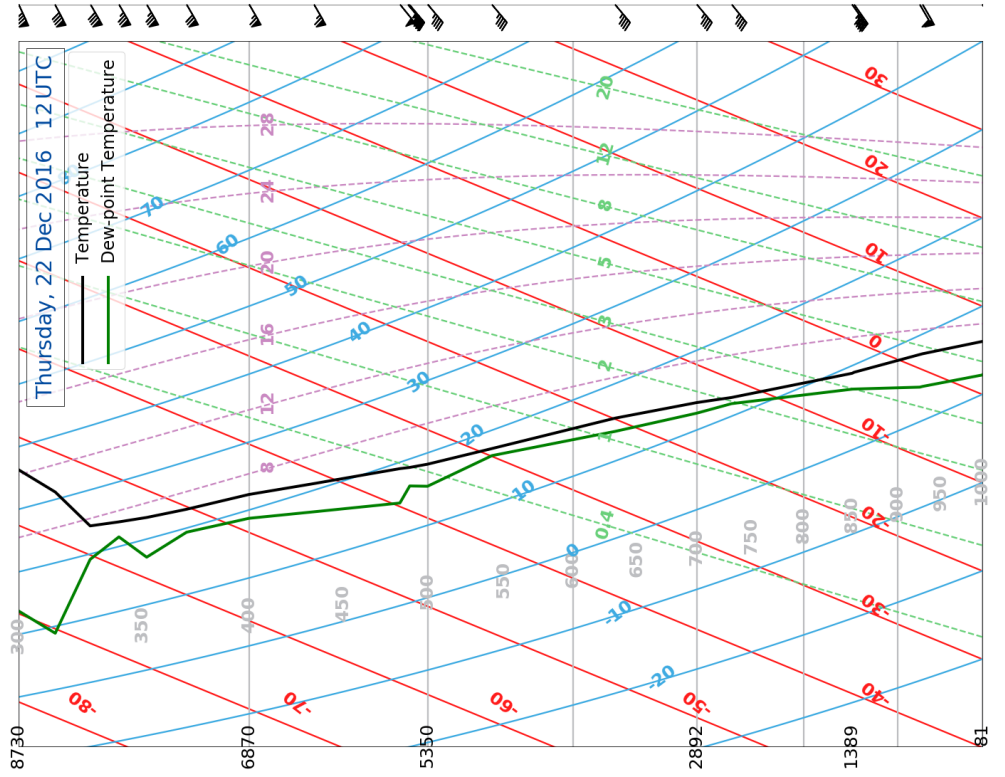
The Skew-T log-P diagram shows the observed vertical temperature and dew-point temperature at Stavanger. The data are taken from ? and processed in Python.

Isobars are grey lines, every 50 hPa, dry adiabats are blue (labelled in $^{\circ}\text{C}$), isotherms are red $[^{\circ}\text{C}]$, water vapour mixing ratios are green, dashed in $[\text{gkg}^{-1}]$, and moist adiabats are dashed, purple lines (labelled in $[^{\circ}\text{C}]$).





(d)



(c)

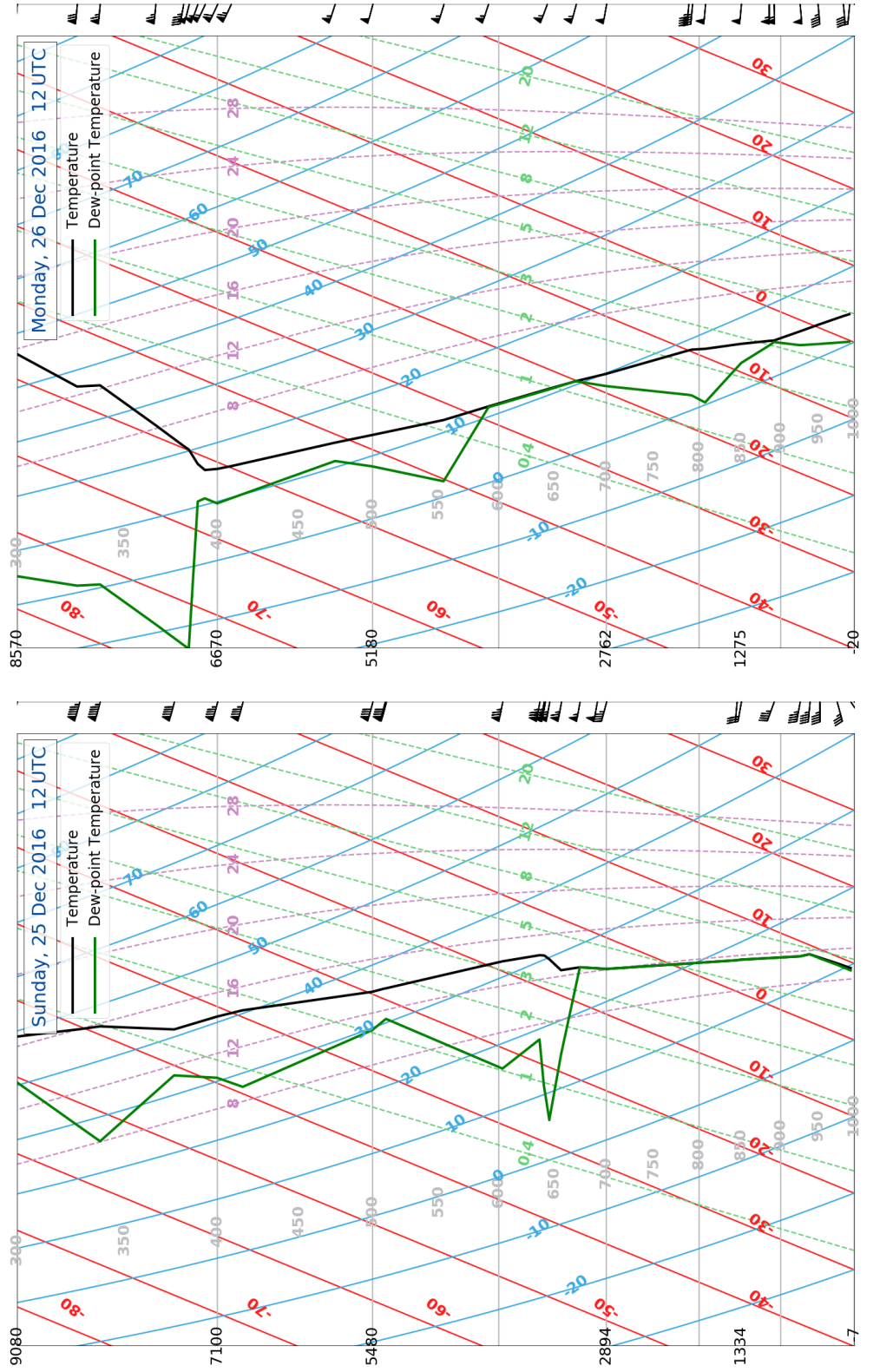
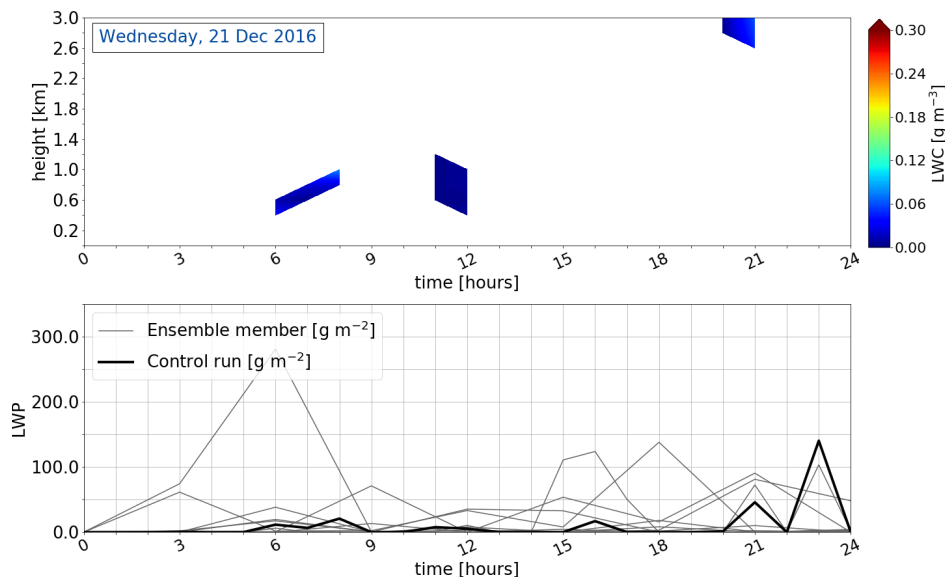
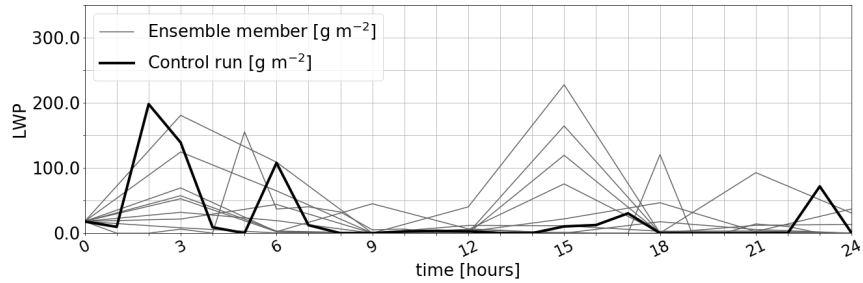
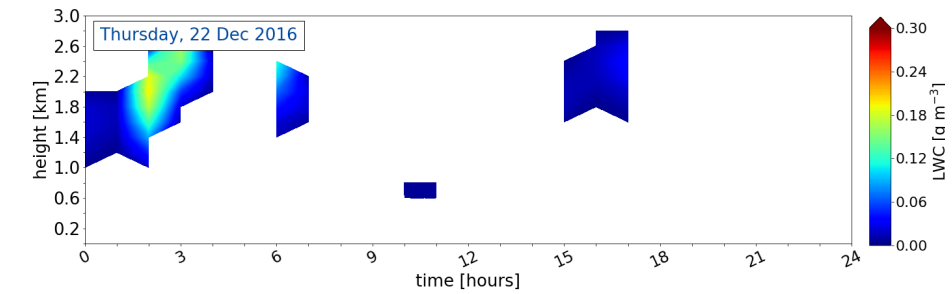


Figure B.0.1: Vertical profiles of atmospheric temperature (black) and dew-point temperature (green) during 20 December 2016 to 26 December 2016. Vertical Profiles from 24 December 2016 are missing at the webpage <http://weather.uwyo.edu/upperair/sounding.html>

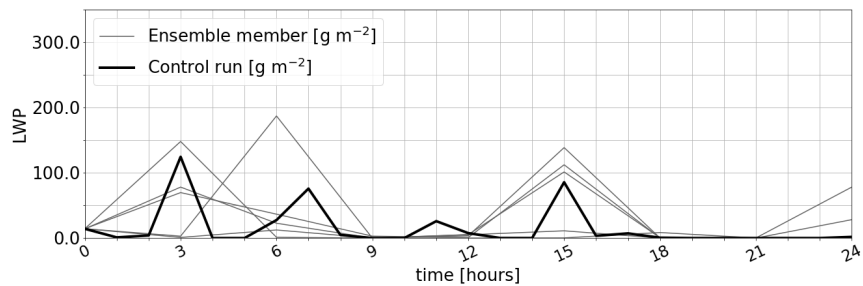
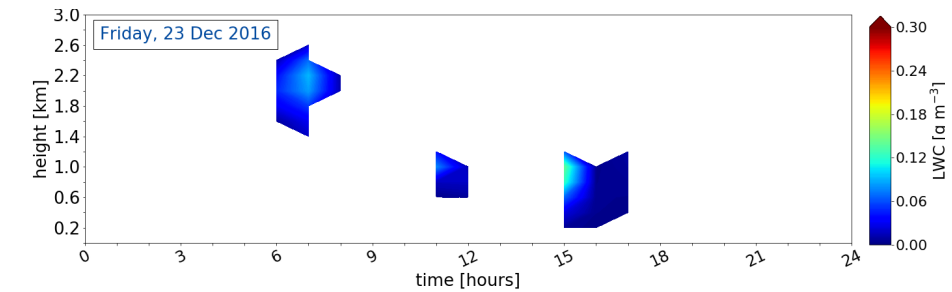
APPENDIX C: LWC FROM MEPS



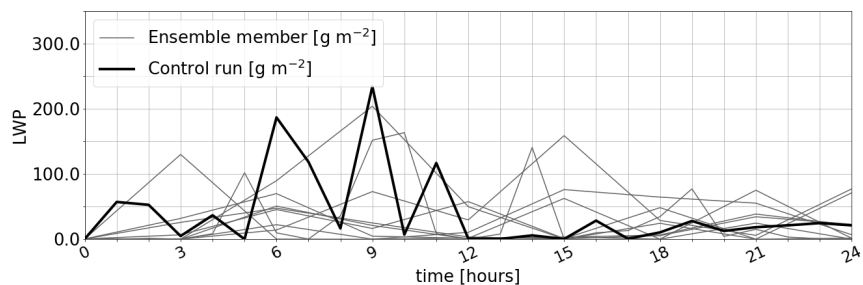
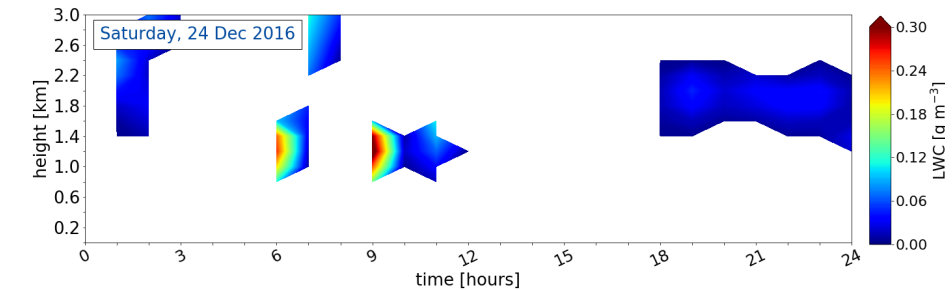
(a)



(b)



(c)



(d)

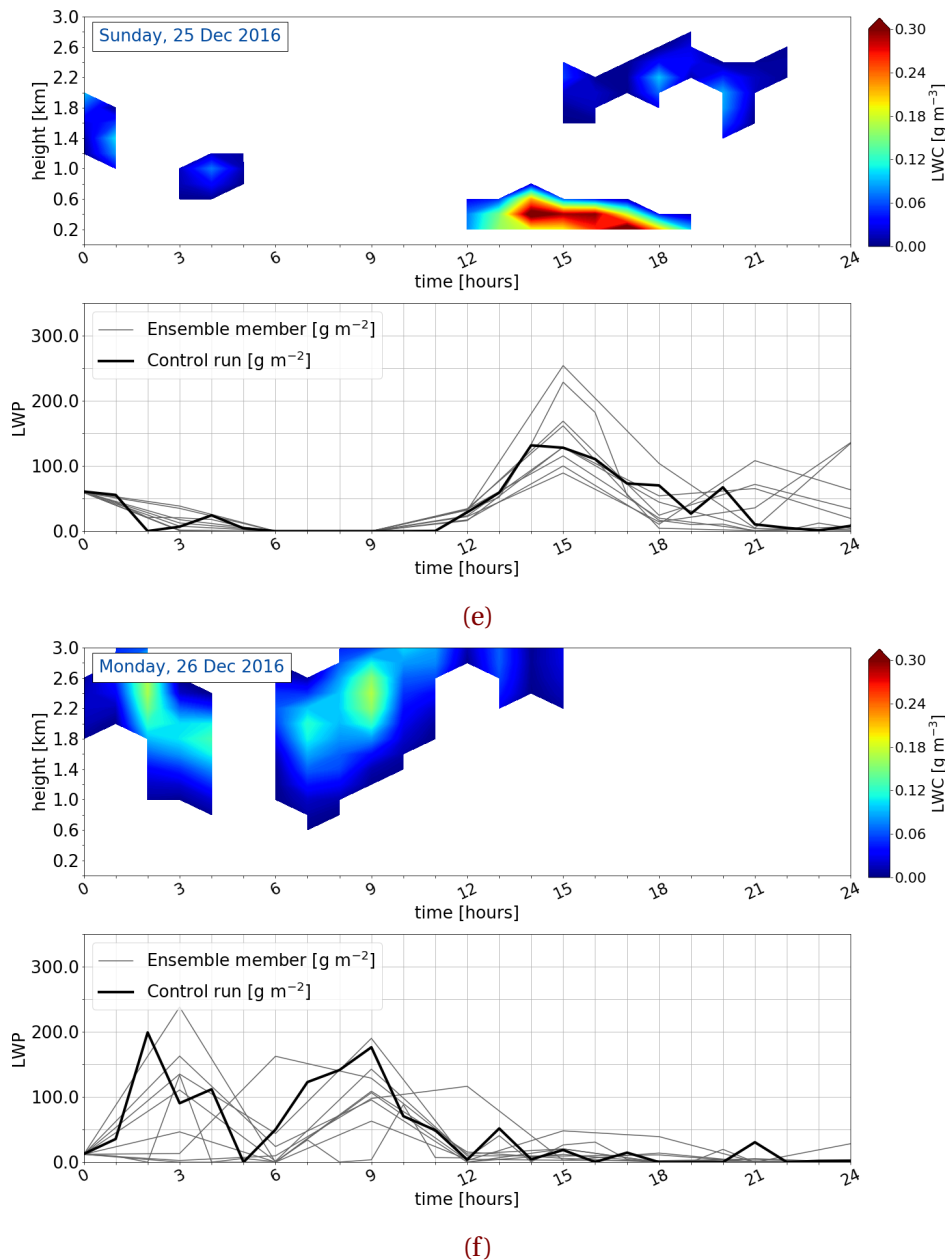


Figure C.0.1: Liquid water content and liquid water path from MEPS.